The host-galaxy response to
the afterglow of GRB 100901A

Citation	Hartoog, O. E., K. Wiersema, P. M. Vreeswijk, L. Kaper, N. R. Tanvir, S. Savaglio, E. Berger, et al. 2013. The Host-Galaxy Response to the Afterglow of GRB 100901A. Monthly Notices of the Royal Astronomical Society 430, no. 4: 2739–2754. doi:10.1093/mnras/stt078.
Published Version	doi:10.1093/mnras/stt078
Citable link	http://nrs.harvard.edu/urn-3:HUL.InstRepos:30456075
Terms of Use	This article was downloaded from Harvard University's DASH repository, and is made available under the terms and conditions applicable to Open Access Policy Articles, as set forth at http://nrs.harvard.edu/urn-3:HUL.InstRepos:dash.current.terms-of-use#OAP

The host-galaxy response to the afterglow of GRB 100901A[*]

Olga E. Hartoog[1,2] †, Klaas Wiersema[3], Paul M. Vreeswijk[4], Lex Kaper[1], Nial R. Tanvir[3], Sandra Savaglio[5], Edo Berger[6], Ryan Chornock[5], Stefano Covino[7], Valerio D'Elia[8,9], Hector Flores[10], Johan P. U. Fynbo[11], Paolo Goldoni[12], Andreja Gomboc[13,14], Andrea Melandri[7,15], Alexei Pozanenko[16], Joop Schaye[2], Antonio de Ugarte Postigo[17], Ralph A. M. J. Wijers[1]

(Affiliations can be found after the references)

18 January 2013

ABSTRACT

For Gamma-Ray Burst 100901A, we have obtained Gemini-North and Very Large Telescope optical afterglow spectra at four epochs: one hour, one day, three days and one week after the burst, thanks to the afterglow remaining unusually bright at late times. Apart from a wealth of metal resonance lines, we also detect lines arising from fine-structure levels of the ground state of Fe II, and from metastable levels of Fe II and Ni II at the host redshift ($z = 1.4084$). These lines are found to vary significantly in time. The combination of the data and modelling results shows that we detect the fall of the Ni II $^4F_{9/2}$ metastable level population, which to date has not been observed. Assuming that the population of the excited states is due to the UV-radiation of the afterglow, we estimate an absorber distance of a few hundred pc. This appears to be a typical value when compared to similar studies. We detect two intervening absorbers ($z = 1.3147, 1.3179$). Despite the wide temporal range of the data, we do not see significant variation in the absorption lines of these two intervening systems.

Key words: gamma-ray burst: individual: GRB 100901A; gamma-rays: bursts - galaxies: abundances - galaxies: ISM - galaxies: distances and redshifts

1 INTRODUCTION

Shortly after the first detection of an optical afterglow associated with a long gamma-ray burst (GRB, van Paradijs et al. 1997), it became clear that GRBs may be useful probes of distant galaxies: afterglows can be very bright and have a simple power law continuum at ultraviolet (UV) to optical wavelengths, against which otherwise undetectable absorbing systems, such as the gas in the host galaxy, leave an observable signature (see e.g., Vreeswijk et al. 2001; Savaglio, Fall & Fiore 2003; Vreeswijk et al. 2004; Berger et al. 2006; Fynbo et al. 2006; Prochaska et al. 2007). Long GRBs are formed as end products of the evolution of massive stars (Woosley 1993; Paczyński 1998) and should therefore probe star-forming regions. Their optical afterglows fade away on short timescales (~days), making it possible to study their host galaxies in emission as well (see e.g.,

Savaglio, Glazebrook & Le Borgne 2009; Hjorth et al. 2012). For a review of long GRBs and their host galaxies, see e.g., Savaglio (2006, 2012).

Optical spectra (i.e., rest frame UV at redshifts around $z \sim 1 - 2$) of GRB afterglows generally show strong absorption lines of metals, both at low and high-ionisation stages, as well as high neutral hydrogen column densities (see Fynbo et al. 2009 for a large and relatively unbiased sample). Absorption lines provide the redshift and allow estimation of column densities of the host galaxy of the GRB and possibly other absorbers along the line of sight. This provides valuable information on the metallicity and dust content of galaxies at arbitrary redshift, regardless of the brightness of these systems, which is very difficult to obtain otherwise. The highest redshift lines in the afterglow spectrum formally only provide a lower limit on the host redshift. However, the presence of fine-structure lines can confirm the galaxy as the host, because these arise from excited states that are expected to have been populated by the UV-afterglow radiation of the GRB (Prochaska, Chen & Bloom 2006; Vreeswijk et al. 2007). These lines are not seen in foreground line-of-sight ab-

sorbers in quasar (QSO) spectra, except for some relatively low-energy excited states from carbon. Due to the transient nature of the afterglow, the absorption lines from these excited states are expected to vary in strength, which may provide information on the internal distribution of gas and kinematics within the host galaxy; often the only way to obtain such information for these distant and mostly faint galaxies. Fine-structure line variation has been measured and modelled for a handful of bursts (e.g., Vreeswijk et al. 2007; Dessauges-Zavadsky et al. 2006; D'Elia et al. 2009a; Ledoux et al. 2009; de Ugarte Postigo et al. 2011; De Cia et al. 2012; Vreeswijk et al. 2013), which allowed constraints to be placed on the distance between the burst and the absorbing material (see Vreeswijk et al. 2013 for a description of the methods used).

The primary difficulty in probing column density variations in GRB sightlines to fit to the models described above, is the requirement on afterglow brightness: for fainter afterglows the necessary high signal-to-noise and high spectral resolution are difficult to obtain with current instrumentation. This also limits this method to early-time data and a limited range of instruments, making it difficult to build up a sample. In the cases described above, the variation is measured with high resolution spectrographs, and all spectra are obtained within a few hours post burst (observer's frame).

The optical afterglow of GRB 100901A remained unusually bright out to very late times, which allowed us to collect spectra over a time span of a week with the Gemini-North Multi-Object Spectrograph and X-shooter on the ESO Very Large Telescope. In this paper we investigate the behaviour of the excited level populations over this unusually long time span, and the application of the excitation models to low and intermediate resolution spectra. The observations and data reduction are described in Section 2. We study the metal resonance lines at the host-galaxy redshift in Section 3.1. In Section 3.1.1 we examine the dust content of the host galaxy. The two intervening absorbers are analysed in Section 3.1.3. In Section 3.2 the fine-structure line variability is described and modelled. In Section 3.3 we briefly discuss the emission lines from the host galaxy. We discuss our results in Section 4 and summarise our conclusions in Section 5.

Throughout the paper we adopt a standard ΛCDM cosmology with $H_0 = 71\,\mathrm{km\,s^{-1}\,Mpc^{-1}}$, $\Omega_m = 0.27$, $\Omega_\Lambda = 0.73$. We indicate line transitions by their vacuum wavelengths.

2 OBSERVATIONS

GRB 100901A was detected by *Swift* on 2010 September 1 at 13:34:10 UT. With a total duration of $T_{90} = 439 \pm 33$ s (Immler et al. 2010; Sakamoto et al. 2010) the burst is clearly classified as a long burst. The optical afterglow candidate at RA (J2000) = $01^h49^m03.42^s$, Dec $= +22°45'30.8''$ (90% confidence error radius of about 0.81″) was identified in an Ultraviolet/Optical Telescope (UVOT) exposure which started 147 s after the Burst Alert Telescope (BAT) trigger (Immler et al. 2010). Automatic observations with the Faulkes Telescope North identified an uncatalogued object at the position consistent with the UVOT candidate (Guidorzi et al. 2010). Several follow-up photometry efforts followed, resulting in the light curve presented and analysed in Gomboc et al. (in prep) and Gorbovskoy et al. (2012) (see also Figure 8). The first optical spectrum of the afterglow was taken with the Gemini Multi-Object Spectrograph (GMOS) on Gemini-North (programme GN-2010B-Q-7, PI Tanvir), approximately 1 hr 15 mins (0.0526 days) after burst trigger (Chornock et al. 2010). With this instrument, two

other spectra at respectively 1 and 7 days after the burst were obtained. A fourth spectrum was obtained approximately 3 days after the burst with the X-shooter spectrograph mounted on the ESO Very Large Telescope (VLT), under programme 085.A-0009(B) (PI Fynbo). See Table 1 for a detailed log of the observations presented in this paper.

2.1 Gemini-N/GMOS spectroscopy

Gemini-N/GMOS is a low-resolution long slit spectrograph, equipped with three detectors. For the observations presented here, a slit width of 0.75″ and the B600 grism with the G5307 order suppression filter have been used, which resulted in the wavelength coverage and resolving power reported in Table 1. We used four exposures per epoch, using dithers in both dispersion and spatial coordinates to sample over the chip gaps and regions affected by amplifier location. The GMOS spectra have been reduced with the IRAF packages for Gemini GMOS (version 1.9), using arc line exposures taken directly before and after the science data. The four exposures are combined after extraction. The resulting spectra were normalised and no flux calibration was performed.

2.2 VLT/X-shooter spectroscopy

VLT/X-shooter is a cross-dispersed échelle spectrograph where the incoming light is split into three wavelength arms using dichroics, covering the full optical to near infrared wavelength range simultaneously (D'Odorico et al. 2006; Vernet et al. 2011). The X-shooter spectra have been taken in nodding mode with 1×2 binning (i.e., binning in the dispersion direction) in the UV-Blue (UVB) and Visual (VIS) arms, using a 100kHz / high-gain readout and 4×600s exposure times. The selected slit widths were 1.0, 0.9 and 0.9″ for the UVB, VIS and near-infrared (NIR) arms, respectively. A 5″ nod throw along the slit was used to improve sky subtraction. The spectra were reduced using the ESO pipeline software version 1.2.2, using the so-called physical model mode (Goldoni et al. 2006; Modigliani et al. 2010). We used calibration data (bias, dark, arc lamp, flat-field and flexure control frames) taken the next day or as close in time as possible to the science observations. The bin sizes of the resulting spectra were 0.2, 0.2, and 0.5Å for UVB, VIS and NIR spectra, respectively. Extracted spectra were flux calibrated using spectrophotometric standard star exposures, also taken the same night, resulting in roughly flux-calibrated spectra spanning the near-ultraviolet to the near-infrared. We caution that the weather conditions during this night were poor, and likely non-photometric. We used a telluric standard star (HD 4670, a B9 V star) to correct the telluric absorption features in the NIR afterglow spectrum, using the IDL SPEXTOOL package (Vacca, Cushing & Rayner 2003, see also Wiersema 2011 for the use on X-shooter data).

3 ANALYSIS

The GMOS epoch1 spectrum (see Figure 1) is that of a bright afterglow including many metal absorption lines. At a redshift of 1.4084 we detect strong resonance lines of Fe II, Mn II, Cr II, Al II, Al III, Zn II and Si II. Additionally, at the same redshift, line transitions arising from excited states of Fe II and Ni II are clearly detected (see Section 3.2). Therefore we identify this as the host-galaxy redshift z_h (Chornock et al. 2010). We do not detect lines from Fe III, as observed in the case of GRB 080310 (De Cia et al. 2012). No
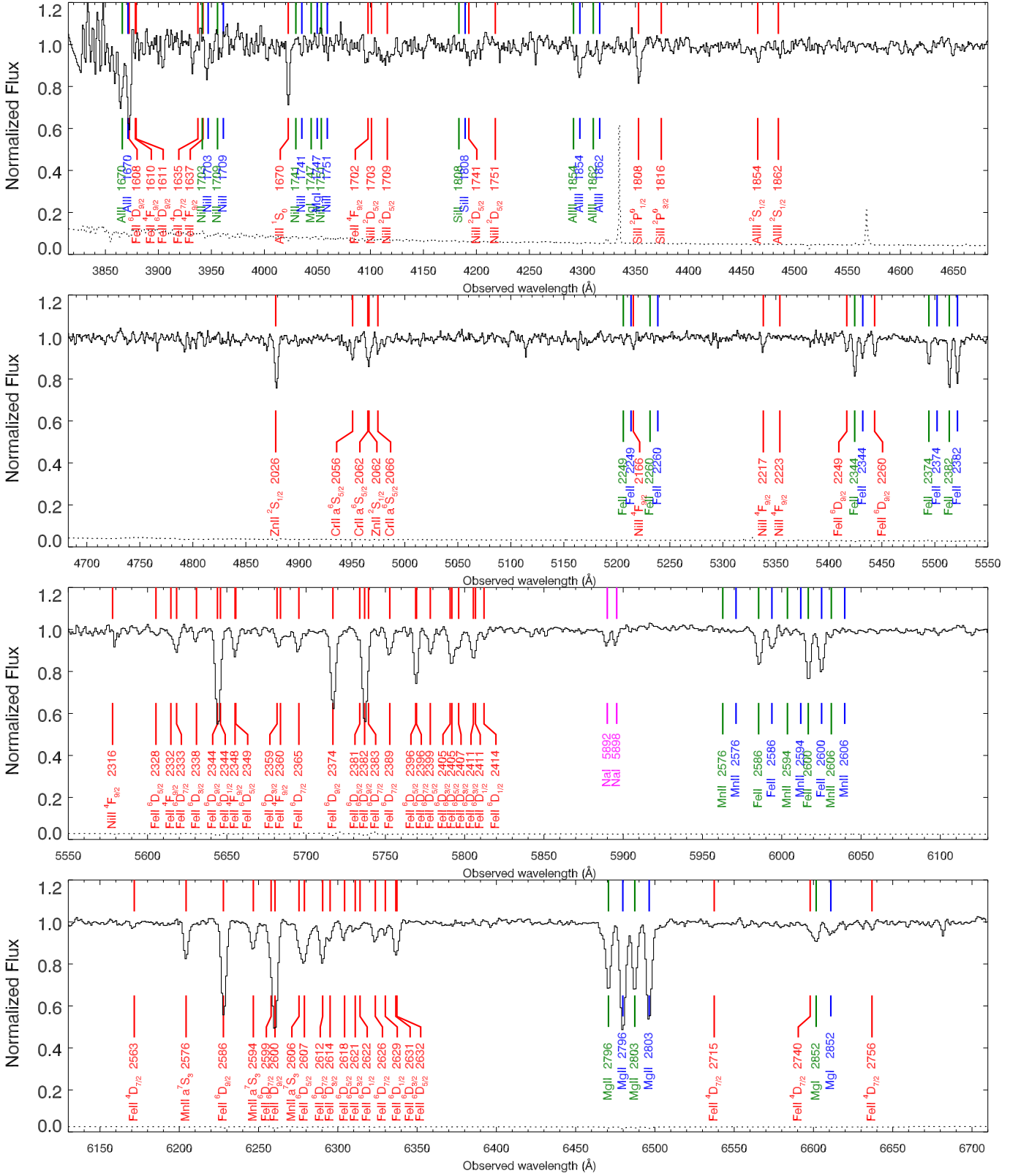
Figure 1. Normalised GMOS spectrum (epoch1) of the afterglow of GRB 100901A. The red labels indicate the absorption lines of the host ($z_h = 1.4084$); the green and blue labels (with vertical offset) indicate the absorption lines formed in two intervening systems at $z_1 = 1.3147$ and $z_2 = 1.3179$. The magenta labels show unshifted Na I lines ($z = 0$), resulting from the absorption in the Milky Way. The numbers at the labels indicate the configuration of the lower level and the vacuum rest wavelength of the transition. The host shows resonance lines from the ions Mn II, Fe II, Cr II, Zn II, Si II, Al II and Al III, as well as lines from excited states of Fe II and Ni II, which are found to vary significantly (see Section 3.2). In the intervening systems we detect Mg I, Mg II, Fe II, Al II and Al III.

Table 1. Overview of the spectroscopic observations of the afterglow of GRB 100901A, arranged by instrument and epoch. Columns (1) and (2) indicate telescope, instrument, setup, and slit dimensions. Column (3) gives the wavelength coverage for this setup and the resolving power $R = \lambda/\Delta\lambda$, with $\Delta\lambda$ the FWHM of an unresolved line. Column (4) gives the mid time of the epochs of observation in days after the burst BAT trigger. Column (5) lists the interpolated observed R-magnitude of the afterglow at this epoch (Gomboc et al., in prep). Column (6) lists the total exposure time of the observation in this epoch. Columns (7) and (8) give the seeing and the airmass. The seeing is measured by fitting a gaussian along the spatial direction of the slit, around the central wavelength of each spectrum. Column (9) gives the signal-to-noise ratio (S/N) in the continuum at 4150 and 6100 Å per GMOS pixel ($\delta\lambda = 0.91$ Å). Column (10) gives the name we will use to refer to the epoch.

Telescope	Instrument and Setup	Spectral Range and Resolution	Time after Burst (days)	m_R	Exp. Time (s)	Seeing ('')	Airmass	S/N/($\delta\lambda = 0.91$Å) at 4150, 6100 Å	Abbrev.
Gemini-North	GMOS,	3810 – 6710 Å	0.0526	17.8	4×400	0.62	1.06	38, 95	epoch1
	B600+ G5307	$R = 1000 - 1900$	1.0095	18.6	4×500	0.52	1.01	16, 70	epoch2
	0.75'' × 330''		7.0270	22.3	4×1200	0.68	1.05	5, 13	epoch3
Very Large Telescope	X-Shooter UVB 1.0'' × 11''	3000 – 25000 Å $R = 5400$	2.7492	20.2	4×600	1.30	1.48	9, 7	xsh
	VIS 0.9'' × 11''	$R = 7400$							
	NIR 0.9'' × 11''	$R = 5800$							

Lyman-α is detected, because it is too far in the blue for the covered wavelength range. Two intervening absorbers are visible at $z_1 = 1.3147$ and $z_2 = 1.3179$ (Chornock et al. 2010). In these systems we detect Fe II, Al II, Al III, Mg I and Mg II (rest frame equivalent width $W_\lambda < 1$ Å). We note that these lines are weaker at the intervening system redshifts than at the host redshift. There are no fine-structure lines detected at any of the intervening absorber redshifts. Na I $\lambda\lambda$ 5892, 5898 are detected at $z = 0$ and are thus due to foreground absorption in the Galaxy.

The GMOS epoch2 spectrum (not fully shown in a figure) looks similar, though the signal-to-noise ratio (S/N) is lower due to the decreasing brightness of the afterglow. The line transitions arising from the metastable Ni II $^4F_{9/2}$ level (see Table A4) appear more pronounced in epoch2 than in epoch1; the Fe II fine-structure lines have become slightly weaker.

Since GMOS epoch3 is observed after the break in the light curve at ~ 2 days (Gomboc et al., in prep), which causes the brightness to drop more quickly, the S/N is lower than for the other epochs, despite the longer integration time and comparable weather conditions. Still, strong metal resonance lines are clearly detected. Fine-structure lines that were present in epoch1 and lines from metastable levels that were present in epoch2 are much weaker or not detected any more (see Section 3.2).

The quality of the X-shooter spectrum (xsh, after 2.75 days, see Table 1) is low due to poor weather conditions and large airmass, but because of the extraordinarily large wavelength coverage of this instrument, this spectrum does provide additional information. Moreover, the higher resolution allow us to exclude the existence of different velocity components down to $\sim 70 \, \mathrm{km \, s^{-1}}$ with respect to $\sim 200 \, \mathrm{km \, s^{-1}}$ for GMOS. The strong and saturated Mg II $\lambda\lambda$ 2796, 2803, Mg I λ 2853, and Ca II $\lambda\lambda$ 3934, 3969 absorption lines from the host galaxy are outside the range of GMOS due to the redshift, but they are clearly detected in xsh-VIS (not shown in a figure). Na I λ 5892, 5897 falls in a region with atmospheric absorption and can therefore not be detected. We do not detect the red wing of the Ly-α absorption line due to low S/N. Furthermore, in xsh-NIR, we marginally detect forbidden oxygen emission line [O III] λ5007 at the host-galaxy redshift (see Figure 9 and Section 3.3).

We do not detect prominent interstellar (dust) extinction features such as the 2175Å feature (see e.g., Elíasdóttir et al. 2009) or diffuse interstellar bands in any of the spectra at the host-galaxy redshift.

3.1 Resonance lines

To measure the observed equivalent width $W_{\lambda,\mathrm{obs}}$ of the absorption lines in the spectrum, we locally fit gaussian functions to the normalised spectrum with NGAUSSFIT, a task in the STSDAS package in IRAF. In principle, $W_{\lambda,\mathrm{obs}}$ can be obtained directly by integration, but as can be seen in Figure 1, many lines are blended. In some cases one line needs to be fixed in order to measure the potential variation of the other. NGAUSSFIT can de-blend up to three lines, with the possibility to keep part of the parameters fixed. This method allows that in spectra with low S/N, an absent or very weak line is sometimes formally best fitted with a line with negative equivalent width (i.e., an emission line, see also Figure 6 and 7); for these lines we obtain upper limits for $W_{\lambda,\mathrm{obs}}$.

The formal error on the equivalent width is obtained from the error spectrum:

$$\sigma W_{\lambda,\mathrm{obs}} = \delta\lambda \sqrt{\sum_i^{\mathrm{line}} (\sigma_i/F_c)^2}, \qquad (1)$$

with $\delta\lambda$ the spectral bin width, σ_i the value of the error spectrum in bin i and F_c the continuum flux. The summation runs over two times the full-width-at-half-maximum (FWHM). Furthermore, we add 3% of the equivalent width to the formal error to account for the uncertainty in placing the continuum. In the low-resolution GMOS spectra, all absorption lines are unresolved and can be fit with a gaussian with a fixed FWHM of 3.6 Å (the resolution element), which is determined from the width of the lines in the arc-lamp frames. In xsh we fix FWHM = 1.0 Å and 0.7 Å in the UVB and VIS-arms, respectively, based on the widths of arc lines and telluric emission lines. Some strongly saturated lines (for example the Mg II doublet) in these spectra cannot be fit with gaussians and are therefore integrated numerically. The resulting rest frame equivalent widths $W_\lambda = W_{\lambda,\mathrm{obs}}/(1 + z_h)$ of the resonance lines in the first two epochs are listed in Table 2.

To infer column densities of the different ions from the absorption line equivalent widths, we make use of a multi-ion single component curve-of-growth (MISC-COG) analysis (Spitzer 1978). The Doppler line width is in principle related to the temperature and the level of turbulence in the absorbing gas. Limited by spectral resolution, it is difficult to distinguish between this and broadening due to the complex physical structure of absorbing clouds in the sight line. Therefore we speak of an 'effective' Doppler parameter, which does not carry information about the temperature of the gas, but is

merely a simplification in the model (Jenkins 1986). The assumption we need to make in this analysis is that the effective Doppler parameter b is the same for all ion species, and that it is single (one velocity component). In other words, we assume that the velocity structure is the same in all lines, and that it is dominated by small-scale effect such as thermal velocities and turbulence and not by differences in bulk velocities of different gas clouds.

3.1.1 Host galaxy column densities

We use three unblended Fe II resonance lines ($\lambda 2249$, $\lambda 2260$ and $\lambda 2586$) to determine b for the line-of-sight gas in the host galaxy (see Table 2). Because these lines cover both the linear and the flat part of the COG, both b and the column density for Fe II, $N_{\mathrm{Fe\,II}}$, can be constrained. They are dependent variables, therefore fit them simultaneously with a grid method, yielding $b = 22.1^{+1.7}_{-1.6}$ km s^{-1} and $\log N_{\mathrm{Fe\,II}}/\mathrm{cm}^{-2} = 15.23^{+0.07}_{-0.08}$.

The COG with the best fit value for b is shown in Figure 2. The ion species other than iron have line transitions either on the linear or on the flat part of the COG; therefore, b has to be assumed to be the same for all ion species in order to determine the column densities. The resulting column densities of the ions are listed in Table 2. For most lines we have taken an average of the first two epochs, except Mg II and Ca II which can only be measured in xsh. The equivalent widths of the Al II lines are slightly larger in epoch1 while those of Al III are larger in epoch2. While not very significant, it may be a sign of ionisation due to the GRB afterglow (see e.g., Vreeswijk et al. 2013). Due to the low significance we decided not to take this into account in the excitation modelling in Section 3.2.

Spectral resolution limits the ability to distinguish different velocity components in absorption lines: an instrumental FWHM = 3.6 Å (GMOS spectra) corresponds to ~ 200 km s^{-1}. In xsh-VIS, a velocity component difference of 70 km s^{-1} would be detectable, but we do not see indications for more than one velocity component in any of the lines. This could be due to the low S/N of xsh, because most intermediate to high-resolution spectra of GRBs show absorption lines with at least two components (but see e.g., Ledoux et al. 2009).

Prochaska (2006) warns that column densities derived with the MISC-COG method are systematically underestimated, especially when the underlying line structure is that of separated clumps of gas at different velocity shifts. In this case one derives a high b with MISC-COG analysis, and therefore a lower column density. Results for a single component COG analysis with $b \gtrsim 20$ km s^{-1} are highly suspect, according to Prochaska (2006). That COG analysis of a low-resolution spectrum can be accurate is shown by D'Elia et al. (2011), who compare low and high-resolution spectra for the afterglow of GRB 081008. The COG analysis gives the same result as line fits to the high-resolution spectrum within 3σ. They conclude that this is linked to the low level of saturation of the lines. The equivalent widths of the low-ionisation lines in GRB 100901A are found to be in the lowest 10% of the sample of 69 low-resolution spectra conducted by de Ugarte Postigo et al. (2012), which strengthens the case that a COG analysis on this spectrum can provide accurate results. However, column densities resulting from COG analysis always need to be treated with caution.
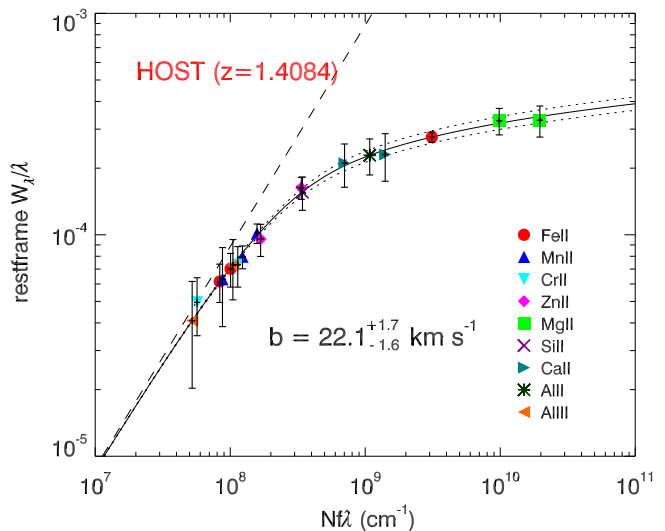

Figure 2. Curve-of-growth (COG) for the resonance lines in the host galaxy of GRB 100901A. The solid line gives the best fit COG with $b = 22.1$ km s^{-1}, the dotted lines show the effect of the error on b. The dashed line, which coincides with the linear part of the COG, is a COG for $b = \infty$, that can be used as an approximation for weak lines.
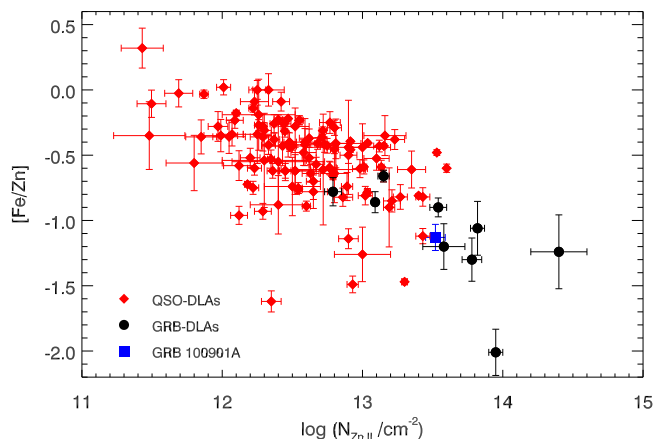

Figure 3. [Fe/Zn] as a function of the Zn II column density in QSO-DLAs (red diamonds), GRB-DLAs (black circles) and GRB 100901A (blue square). QSO-DLA values are from Lu et al. (1996); Prochaska & Wolfe (1996, 1997); Pettini et al. (1999, 2000); Prochaska & Wolfe (2000); Prochaska et al. (2001). GRB-DLA values are from Savaglio, Fall & Fiore (2003); Fynbo et al. (2002); Fiore et al. (2005); Watson et al. (2006); Penprase et al. (2006); Vreeswijk et al. (2007); D'Elia et al. (2009b, 2011).

3.1.2 Dust depletion

The strength of the absorption lines in the spectrum are a measure of the abundance of an element in the gas phase only. Apart from the overall gas-to-dust ratio, the fraction of a specific element that is locked onto dust depends on the element species and on the nature of the dust. Therefore, the pattern of relative abundances, the depletion pattern, might give insight into the amount and nature of the dust. In Table 2 we list the abundance ratios with respect to the refractory (depleted) element Fe and the non-refractory element Zn, compared to the ratio in a solar abundance environment. We use the following, commonly used notation

Table 2. The measured rest-frame equivalent width W_λ for the resonance lines at the host redshift, and the corresponding ion column densities, obtained with curve-of-growth (COG) analysis. The first column lists the ion and the vacuum rest wavelength (Å); the second column gives the oscillator strength f_λ. Columns (3) and (4) give the rest-frame W_λ in Å measured in epoch1 and epoch2 (GMOS) respectively. For lines for which we have a good measurement both in epoch1 and epoch2, the weighted average is used; otherwise we use the value measured in epoch1. The values that are finally used for the COG analysis are listed in Column (5). Column (6) gives the best fitting column density for the ion, fitted to a COG with effective Doppler parameter $b = 22.1^{+1.7}_{-1.6}$ km s^{-1}. Columns (7) and (8) give the relative abundances with respect to iron and zinc using solar values from Asplund et al. (2009) (for notation see Equation 2). The references for the wavelength and oscillator strength are in column (9).

Line	f_λ	$W_\lambda/$Å epoch1	$W_\lambda/$Å epoch2	$< W_\lambda/$Å $>$	$\log(N_\text{ion}/\text{cm}^{-2})$	[X/Fe]	[X/Zn]	ref
Al II 1670.7874	1.740	0.418 ± 0.093	0.338 ± 0.098	0.380 ± 0.067	$13.57^{+0.41}_{-0.32}$	-0.61 ± 0.42	-1.84 ± 0.42	1
Al III 1854.7164	0.539	0.113 ± 0.054	0.162 ± 0.060	0.135 ± 0.040	$13.02^{+0.13}_{-0.16}$	a	a	1
Al III 1862.7895	0.268	0.044 ± 0.051	0.113 ± 0.056	0.075 ± 0.038	...			1
Si II 1808.013	2.080×10^{-3}	0.292 ± 0.062	0.267 ± 0.068	0.281 ± 0.046	$15.96^{+0.18}_{-0.16}$	$+0.72 \pm 0.19$	-0.51 ± 0.19	2
Zn II 2026.136^b	5.010×10^{-1}	0.362 ± 0.046	0.280 ± 0.053	0.327 ± 0.035	$13.52^{+0.07}_{-0.07}$	$+1.23 \pm 0.10$		3
Zn II 2062.664	2.460×10^{-1}	0.191 ± 0.041	0.206 ± 0.048	0.197 ± 0.031	...			3
Cr II 2056.2539	1.030×10^{-1}	0.150 ± 0.040	0.151 ± 0.046	0.151 ± 0.030	$13.73^{+0.09}_{-0.10}$	$+0.36 \pm 0.12$	-0.87 ± 0.12	3
Cr II 2066.161	5.120×10^{-2}	0.096 ± 0.038	0.111 ± 0.045	0.102 ± 0.029	...			3
Fe II 2249.8754^c	2.190×10^{-3}	0.129 ± 0.034	0.151 ± 0.040	0.139 ± 0.026	$15.23^{+0.07}_{-0.08}$		-1.23 ± 0.10	4
Fe II 2260.7793	2.620×10^{-3}	0.152 ± 0.034	0.168 ± 0.040	0.159 ± 0.026	...			4
Fe II 2586.6495	7.094×10^{-2}	0.705 ± 0.044	0.727 ± 0.048	0.715 ± 0.032	...			4
Mn II 2576.877	3.610×10^{-1}	0.265 ± 0.032	0.257 ± 0.037	0.262 ± 0.024	$13.23^{+0.04}_{-0.05}$	$+0.07 \pm 0.09$	-1.16 ± 0.04	5
Mn II 2594.499	2.800×10^{-1}	0.206 ± 0.030	0.207 ± 0.034	0.207 ± 0.023	...			5
Mn II 2606.462	1.980×10^{-1}	0.164 ± 0.064	d	0.164 ± 0.064	...			5
Mg II 2796.352	6.123×10^{-1}			0.920 ± 0.147^e	$15.06^{+0.83}_{-0.60}$	-0.27 ± 0.83	-1.50 ± 0.83	6
Mg II 2803.531	3.054×10^{-1}			0.918 ± 0.126^e	...			6
Ca II 3934.777	6.500×10^{-1}			0.907 ± 0.220^e	$13.74^{+0.47}_{-0.50}$	-0.33 ± 0.50	-1.56 ± 0.50	7
Ca II 3969.591	3.220×10^{-1}			0.836 ± 0.185^e	...			7

^{a}The quantities [Al III/Fe] and [Al III/Zn] do not have any physical meaning, since the Al III is probably mainly from a different region than Al II, Fe II and Zn II (see also Savaglio & Fall 2004).

^{b}The contamination by Cr II $\lambda2026$ is determined from the other Cr II lines and is negligible. The contribution of Mg I $\lambda2026$ cannot be determined, but we assume it is small based on the absence of Mg I $\lambda1827$.

^{c}Fe II 2344, 2374, 3282 and 2600 are also clearly detected, but those are blended with fine-structure lines and therefore not used in the abundance study. Estimates of their equivalent widths can be found in the appendix.

^{d}The equivalent width of the line is fixed in the second epoch in order to measure the varied strength of the blended fine-structure line(s).

^{e}Absorption lines are outside the GMOS range, measurement is from xsh spectrum.

References for atomic data: (1) NIST Atomic Spectra Database, (2) Bergeson & Lawler (1993b), (3) Bergeson & Lawler (1993a) (4) Verner et al. (1999), (5) Morton (2003), (6) Verner et al. (1996), (7) Morton (1991).

$$[X/Y] \equiv \log\left(\frac{N(X)}{N(Y)}\right) - \log\left(\frac{n(X)}{n(Y)}\right)_\odot, \qquad (2)$$

with $N(X)$ the column density of element X, and $n(X)$ the number density of element X in a solar environment (Asplund et al. 2009). Differences from zero indicate dust content. We thus assume that relative abundances (both in gas and dust) are solar. Fe, Zn and Cr are iron peak elements, which makes this a reasonable assumption, although the main production pathway of Zn is not fully identified (Umeda & Nomoto 2002). Discrepancies in relative abundances might also be due to a different star-formation history than the Milky Way.

In Figure 3 we show [Fe/Zn] as a function of the Zn column density for the host of GRB 100901A, compared with a sample of other GRB-DLAs and QSO-DLAs[1]. The relative abundance values indicate a stronger depletion (i.e., more dust) in GRB-DLAs than in QSO-DLAs, but among the GRB-DLAs, GRB 100901A is not a particularly special case. Both GRB-DLAs and QSO-DLAs appear to follow the overall trend that systems with stronger Zn column densities show stronger depletion. The fact that the two classes populate different regions in the diagram is mainly a sight line effect. QSOs probe galaxies in random orientations with only a small chance that the densest region of a galaxy is intersected, while sight lines to GRB afterglows probe the gas towards the progenitor region, so they will in general show high column densities (see also Savaglio 2006; Prochaska et al. 2007; Fynbo et al. 2009).

[1] DLA: Damped Lyman-α system: a sight line absorber with $N_{HI} > 2 \times 10^{20}$ cm^{-2} (Wolfe, Gawiser & Prochaska 2005). A DLA system in a GRB afterglow spectrum is usually due to the host galaxy.

Furthermore, for GRB-DLAs with relatively low column densities and weak absorption lines, [Fe/Zn] is not well constrained (i.e., not reported in literature) because the fading afterglow prevents building up S/N over several nights of observations. This is not the case for QSO-DLAs, which is why these objects also populate the low $N_{Zn\,II}$ part of the parameter space.

A more detailed analysis of the dust content can be performed by comparing the heavy-element dust depletion pattern of GRB 100901A with observations in the interstellar medium (ISM) of the Milky Way (Savage & Sembach 1996). We use the method described in Savaglio & Fall (2004). We consider the observed depletion patterns in the MW sight lines trough a warm halo (WH), warm disk and halo (WDH), warm disk (WD) and cool disk (CD) as models. For the fit, we use two free parameters. One is the dust-to-metal ratio relative to the Galactic values $\kappa = \kappa_{GRB}/\kappa_J$ (J is one of the 4 depletion patterns). The second is proportional to the metallicity (not known because N_{HI} is not measured in GRB 100901A). The two parameters are scaled until they reproduce the observed heavy-element depletion pattern best (minimum χ^2).

Results using measurements of 7 elements are shown in Figure 4. The WH depletion pattern gives the smallest χ^2 among the 4 patterns, but the WD pattern is also a reasonable fit. The dust-to-metals ratio is between the MW value and 10% higher. Ni and Mg are the most uncertain measurements. The Mg II column density is likely a lower limit because it suffers from very strong saturation. The Ni II column density is not measured from the resonance lines directly, but follows from the modelling of the time evolution of the Ni II $^4F_{9/2}$ metastable level (see Section 3.2.1 and Table 5). Excluding these two elements from the fit does not change our results much.

For the observed column of metals, and assuming a rate of visual extinction per column density of metals like in the MW (Bohlin, Savage & Drake 1978), the expected optical extinction in GRB100901A would be $A_V \sim 0.5$. This is higher than the one derived from the spectral energy distribution (SED) of GRB100901A ($A_V = 0.21$, Gomboc et al., in prep). This inconsistency is typically observed in GRB sight lines (Schady et al. 2011) and indicates that the rate of extinction in the ISM of GRB hosts per column of metals is different from what is observed in the MW.

3.1.3 Intervening absorbers

Two intervening absorbers are detected: int1 at $z_1 = 1.3147$ and int2 at $z_2 = 1.3179$. If these two systems are not physically associated with each other, and the redshift difference is dominated by cosmological expansion, the velocity difference corresponds to a co-moving separation of 3.9 Mpc. If the absorbers belong to one system, the velocity difference is $414 \, \mathrm{km \, s^{-1}}$, and could be due to motion of galaxies within a cluster.

Because of the long time span that our observations cover (until long after the jet break, Gomboc et al., in prep), the data set is suited to look for variations in the strength of the lines from the intervening absorbers. This can be interesting in the context of the previously supposed discrepancy between the number of strong Mg II absorbers ($W_\lambda(2796) > 1$Å) in QSO and GRB sight lines; in the latter the redshift number density was found to be about two times as high (Prochter et al. 2006; Vergani et al. 2009; Cucchiara et al. 2009. However, Cucchiara et al. (2012) used a larger sample and did not reproduce this discrepancy.

We do not detect variability above the 2σ level in any of the two intervening absorbers of GRB 100901A, and we see no
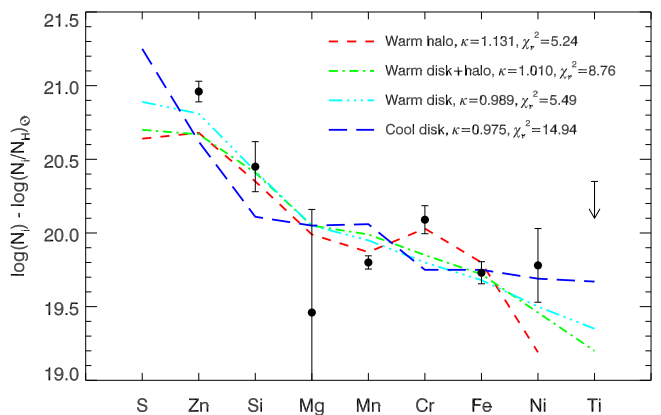
Figure 4. Depletion pattern for the host of GRB 100901A, compared with different components in the Milky Way (Savage & Sembach 1996), which are observed patterns that can be adjusted by changing the dust-to-metal ratio κ. The column density of Ni II is not directly measured but follows from the modelling of the fine-structure and metastable levels, see Section 3.2.1. We include a 3σ upper limit for Ti II based on the absence of the doublet at a rest wavelength of 1910 Å.
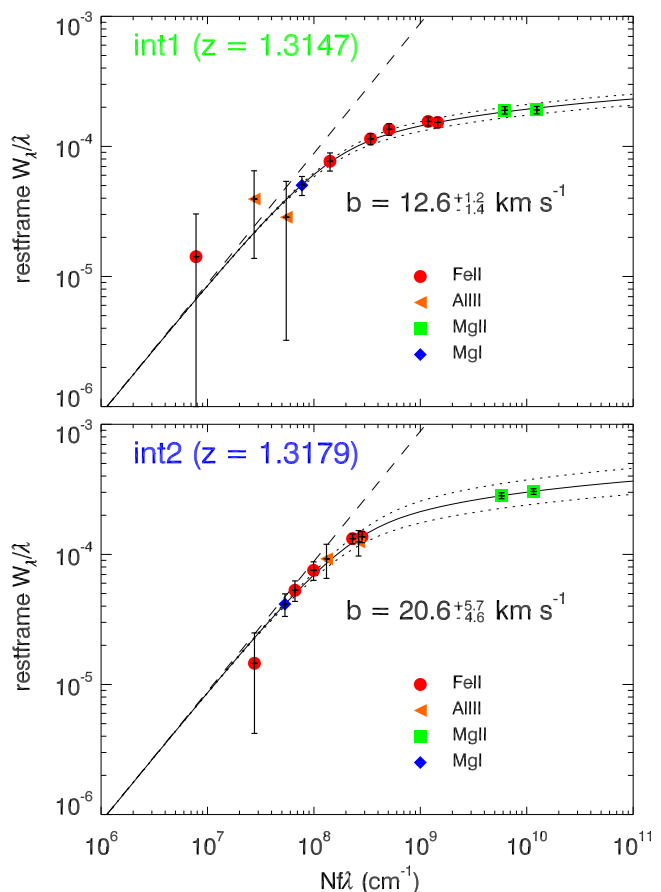
Figure 5. Curve-of-growth for the two intervening systems in the sightline to GRB 100901A. The lines used and the best-fit column densities are listed in Table 3.

systematic trend in the ensemble of lines per absorber, nor per ion species. In principle, the non-variation of the equivalent widths of the intervening absorber resonance lines gives a lower limit on the size of the absorbing clouds (i.e., the scale on which the absorbing gas is homogeneous). If the projected apparent size of the afterglow became larger than the projected size of the intervening absorber, the absorption lines from this system would become weaker since part of the light would reach the observer unabsorbed. We use the description of the apparent size of the Blandford-McKee spherical expansion described by Granot, Piran & Sari (1999), where we use $E_{iso} = 6.3 \times 10^{52}$ erg (Gorbovskoy et al. 2012). We assume the close circum-burst medium to have a constant density $n = 1 \, \text{cm}^{-3}$. At the time of the last epoch (7.027 days), we find the source to be 9.6×10^{16} cm. This gives a lower limit on the size of each of the absorbing clouds of 0.03 pc. Although this is not a very meaningful lower size-limit for a gas cloud, we point out that in general it is difficult to put limits on absorber sizes, but see D'Elia et al. (2010a) for methods applied to GRB absorbers and Petitjean et al. (2000); Ellison et al. (2004); Balashev et al. (2011) for examples of size estimates of QSO line-of-sight objects.

Because the lines of the intervening systems do not vary in strength, we can average the equivalent widths measured in epoch1 and epoch2. The MISC-COG analysis can be applied, because we detect many clear lines from these systems. Figure 5 shows the best fitting COGs for both intervening absorbers. We carry out the same approach as for the host, by first constraining b with the Fe II transitions. We find $b = 12.6^{+1.2}_{-1.4}$ km s^{-1} for int1 and $b = 20.6^{+5.7}_{-4.6}$ km s^{-1} for int2. The equivalent widths and the column densities of each ion species are listed in Table 3.

3.2 Detection and variability of transitions arising from excited levels of Fe II and Ni II.

At the redshift of the host galaxy we detect lines from fine-structure levels of Fe II ($^6D_{7/2}$, $^6D_{5/2}$, $^6D_{3/2}$ and $^6D_{1/2}$) and metastable levels of Fe II ($^4F_{9/2}$ and $^4D_{7/2}$) and Ni II ($^4F_{9/2}$). The equivalent width of many of these lines varies with time. This provides the opportunity to derive the distance between the burst location and the absorbing material, assuming that the population of these excited states is due to the UV-radiation of the afterglow (see Section 3.2.1). With high-resolution spectra it would be possible to directly measure the column densities of the ions that are in the excited states, via Voigt profile fits to the fine-structure lines (see e.g., D'Elia et al. 2007; Vreeswijk et al. 2007). In order to obtain column densities from the equivalent widths, we need to take an intermediate step with the COG, where we fix b to the value found from the resonance Fe II lines (see Section 3.1.1); i.e., we assume that the ions in the excited states are in the same absorbing clouds as the ions in the ground state; for the implications of this assumption see the end of Section 3.2.1. Note that the value of b will only have a very small influence on the column densities of the excited ions, because the lines are all weak and lie mostly on the linear part of the COG.

Tables A1, A2, A3 and A4 in the Appendix give an overview of all transitions from the fine-structure and metastable levels of Fe II and Ni II that would in principle be observable in the GMOS spectral range at this redshift. Due to the low spectral resolution, many of these lines are blended such that the individual variation of the components cannot be measured. The lines that are used in the modelling are shown in boldface in Tables A1 to A4.

In order to obtain the column density N_{level} of ions in a specific

excited state in an epoch, the equivalent widths of the transitions arising from this excited level are placed on the COG by assigning an N_{level} to this level. The best-fit N_{level} is the value for which the ensemble of transitions fit the COG best (minimisation of the χ^2). Figures 6 and 7 show the COG of the Ni II $^4F_{9/2}$ and the Fe II $^6D_{7/2}$ level per epoch (columns), together with the observed transitions from this level and gaussian fits to the line profiles. The best-fit N_{level} and its errors are found with a Monte Carlo simulation, which we apply as follows. In every iteration, for each transition an equivalent width is randomly picked from a normal distribution with as mean the measured value and as sigma the measured error. For this simulated ensemble of equivalent widths, the best-fit N_{level} is determined by minimising the χ^2. After 10 000 iterations, the distribution of best-fit N_{level}'s is fit with an asymmetric gaussian (i.e., a normal distribution with a different σ on both sides), from which we derive the overall best N_{level} and its lower and upper 1σ error. Because the fine-structure lines lie mostly on the linear part of the COG, the effect of b is small, and the uncertainty of this value is not taken into account. If two or more transitions of a level are detected in an epoch (i.e., if $|W_\lambda| > \sigma|W_\lambda|$), we obtain a value for N_{level}, otherwise we obtain an upper limit (see Table 4).

3.2.1 UV-pumping models

The column densities of the fine-structure and metastable states are found to vary in time (see Table 4 and Figure 8). The presence, and variation, of fine-structure lines in GRB afterglow spectra can generally well be explained by excitation due to the UV flux of the GRB afterglow. Prochaska, Chen & Bloom (2006) suggest that this is the dominant excitation mechanism, especially when variability is measured. The early high-resolution spectroscopic data obtained for GRB 060418 (Vreeswijk et al. 2007) allowed systematic tests of other excitation mechanisms such as a background IR field and collisional excitation, but also strongly favours the UV-pumping scenario. For GRB 100901A we assume that UV-pumping is the only relevant photo-excitation mechanism.

We apply the photo-excitation model introduced by Vreeswijk et al. (2007, 2011, 2013). For technical details we refer to the 2013 paper. The general idea is that the UV-flux of the afterglow temporarily excites ions in a cloud with thickness l at a distance d from the location of the burst. As the afterglow brightness fades in time, the excited levels depopulate after a time which is determined by the Einstein coefficient A_{ul} or, equivalently, the oscillator strength of the transitions considered. For a given set of input parameters, the column density of each excited level as a function of time, $N_{level}(t)$, is predicted by the model. By comparing this temporal behaviour to the measured $N_{level}(t)$ for all levels simultaneously, we can optimise the parameters.

The afterglow flux is included as an interpolated series of R-band magnitudes[2] $m_R(t)$ (see upper panel Figure 8), which corresponds to the rest-frame UV-flux (at ~ 2700 Å) responsible for populating the levels. The monochromatic flux in the host-galaxy rest frame at the GRB-facing side of the absorbing cloud is computed as follows:

$$F_\nu^{rest}(t) = \frac{F_0 \cdot 10^{[m_R(t)-A_{R,gal}]/-2.5}}{1+z_h} \left[\frac{\lambda_{rest}(1+z_h)}{6415 \, \text{Å}}\right]^{\beta_\nu} \left[\frac{D_L}{d}\right]^2 \qquad (3)$$

---

[2] The observed R-band magnitudes come from GCNs Andreev, Sergeev & Pozanenko (2010a,b,c,d); Andreev et al. (2010); Kuroda et al. (2010a,b); Volnova et al. (2010); assembled by Gomboc et al. (in prep.).

Table 3. The rest-frame equivalent widths W_λ for the lines from two intervening systems int1 and int2 at respectively $z_1 = 1.3147$ and $z_2 = 1.3179$. $< W_\lambda/\text{Å} >$ is the weighted average of the rest frame equivalent width (in Ångstrom) measured in GMOS epoch1 and epoch2. The COGs for the two systems are shown in Figure 5. The column densities per ion species have been calculated with the COG with the best fitting b; the errors on the column densities are the result of taking into account the range in b. Especially for lines on the flat part of the COG (e.g., Mg II), the effect on N due to b is large.

Line	f_λ	int1 ($z_1 = 1.3147$) $b = 12.6^{+1.2}_{-1.4}$ km s^{-1} $< W_\lambda/\text{Å} >$	$\log(N_{\text{ion}}/\text{cm}^{-2})$	int2 ($z_2 = 1.3179$) $b = 20.6^{+5.7}_{-4.6}$ km s^{-1} $< W_\lambda/\text{Å} >$	$\log(N_{\text{ion}}/\text{cm}^{-2})$
Al III 1854.7164	0.539	0.053 ± 0.046	$12.74^{+0.29}_{-0.43}$	0.229 ± 0.049	$13.42^{+0.27}_{-0.17}$
Al III 1862.7895	0.268	0.073 ± 0.047	...	0.171 ± 0.049	...
Fe II 2249.8754	2.190×10^{-3}	0.032 ± 0.036	$14.28^{+0.15}_{-0.09}$	a	
Fe II 2344.2129	1.252×10^{-1}	0.317 ± 0.030	...	0.176 ± 0.027	$13.57^{+0.09}_{-0.08}$
Fe II 2374.4604	3.297×10^{-2}	0.182 ± 0.028	...	0.034 ± 0.024	...
Fe II 2382.7641	3.432×10^{-1}	0.365 ± 0.030	...	0.325 ± 0.029	...
Fe II 2586.6495	7.094×10^{-2}	0.296 ± 0.027	...	0.136 ± 0.023	...
Fe II 2600.1722	2.422×10^{-1}	0.405 ± 0.028	...	0.344 ± 0.027	...
Mg II 2796.352	6.123×10^{-1}	0.532 ± 0.030	$14.86^{+0.26}_{-0.47}$	0.845 ± 0.035	$14.83^{+1.39}_{-0.68}$
Mg II 2803.531	3.054×10^{-1}	0.531 ± 0.030	...	0.792 ± 0.034	...
Mg I 2852.9642	1.83	0.143 ± 0.023	$12.17^{+0.09}_{-0.11}$	0.118 ± 0.022	$12.01^{+0.09}_{-0.11}$

^{a}this line is blended with Ni II $^4F_{9/2}$ $\lambda2166.23$ at the host redshift.

Table 4. Lower level column densities $\log\left(N_{\text{level}}(t)/\text{cm}^{-2}\right)$ for Fe II and Ni II excited states derived from fine-structure line equivalent widths with COG analysis. All errors and limits are 1σ.

	time (d)	Fe II $^6D_{9/2}$	$^6D_{7/2}$	$^6D_{5/2}$	$^6D_{3/2}$	$^6D_{1/2}$	$^4D_{7/2}$	Ni II $^4F_{9/2}$
epoch1	0.0526	$15.20^{+0.08}_{-0.09}$	$13.77^{+0.05}_{-0.04}$	$13.58^{+0.06}_{-0.10}$	$13.30^{+0.07}_{-0.09}$	$12.92^{+0.11}_{-0.14}$	$12.54^{+0.11}_{-0.18}$	$13.25^{+0.10}_{-0.15}$
epoch2	1.0095	$15.29^{+0.07}_{-0.10}$	$13.68^{+0.05}_{-0.05}$	$13.46^{+0.05}_{-0.13}$	$13.14^{+0.09}_{-0.15}$	< 12.83	$12.54^{+0.11}_{-0.24}$	$13.73^{+0.07}_{-0.12}$
xsh	2.7492	$15.16^{+0.12}_{-0.18}$	< 13.46	< 14.02	< 13.47	< 13.40	< 13.03	$13.54^{+0.09}_{-0.13}$
epoch3	7.0270	$15.34^{+0.21}_{-0.48}$	< 13.37	< 13.80	< 13.39	< 13.47	< 12.97	< 13.75

in which $F_0 = 3.02 \times 10^{-20}$ erg s^{-1} cm^{-2} Hz^{-1} is the flux of Vega at the effective wavelength (6410 Å) of the *R*-band (Fukugita, Shimasaku & Ichikawa 1995), $A_{R,\text{gal}} = 0.264$ is the Galactic extinction (Schlegel, Finkbeiner & Davis 1998), λ_{rest} is the wavelength array of the relevant transitions at which the flux is required to calculate the amount of excitation, β_ν is the spectral slope and $D_L = 9.968 \times 10^9$ pc is the luminosity distance. The effective Doppler parameter b is fixed to 22.1 km s^{-1}, consistent with how we converted equivalent widths to column densities (see Section 3.2). Parameters that can be constrained from the light curve and/or SED fitting (Gomboc et al., in prep) are kept fixed: optical spectral slope $\beta_\nu = 0.82$, and optical extinction in the host galaxy $A_V = 0.21$ assuming a Small Magellanic Cloud extinction profile (Gomboc et al., in prep). We performed models with $A_V = 0$ as well to study the effect. A_V is not included in Equation 3 because the model allows to specify where the optical extinction takes place. We place the extinction in the absorbing cloud, and apply the necessary corrections to the flux.

Table 5 shows the fit results of the model to the measured $N_{\text{level}}(t)$ as listed in Table 4, with different requirements for the parameters. The model without extinction fits the data best with a small cloud at ~ 250 pc, but when we include optical extinc-

tion $A_V = 0.2$, the data favours a configuration with a very large (> 1 kpc) absorbing cloud at a smaller distance. Fixing the cloud size l leads to absorber distances of $d \sim 165 - 275$ pc. Figure 8 shows the fit to the data for the model with $l \leqslant 500$ pc (solid lines) and the model with $l = 1$ pc (dotted lines). Both models are decent fits: our data are not constraining enough to discriminate between the close-large and the distant-small cloud case. But in all cases, the influence of the GRB reaches distances of a few hundreds of parsecs. In Section 4.1 we will discuss the implications of this estimated absorber distance and compare it to values found in other GRBs.

Though not detectable with the spectral resolution used, it could be possible that ground-state Fe II is present in more velocity components than excited Fe II, i.e., that there is Fe II that is not associated with the excited gas. If there exists more Fe II further away, then this would decrease the amount of Fe II that is associated with the excited Fe II, and hence this would move the absorber closer to the burst, i.e., we would infer a smaller GRB-absorber distance. Very roughly, if this fraction of Fe II associated to excited Fe II is only 50% (rather than the now assumed 100%), then it would decrease the distance by a factor of $\sqrt{2}$. So even when assuming such
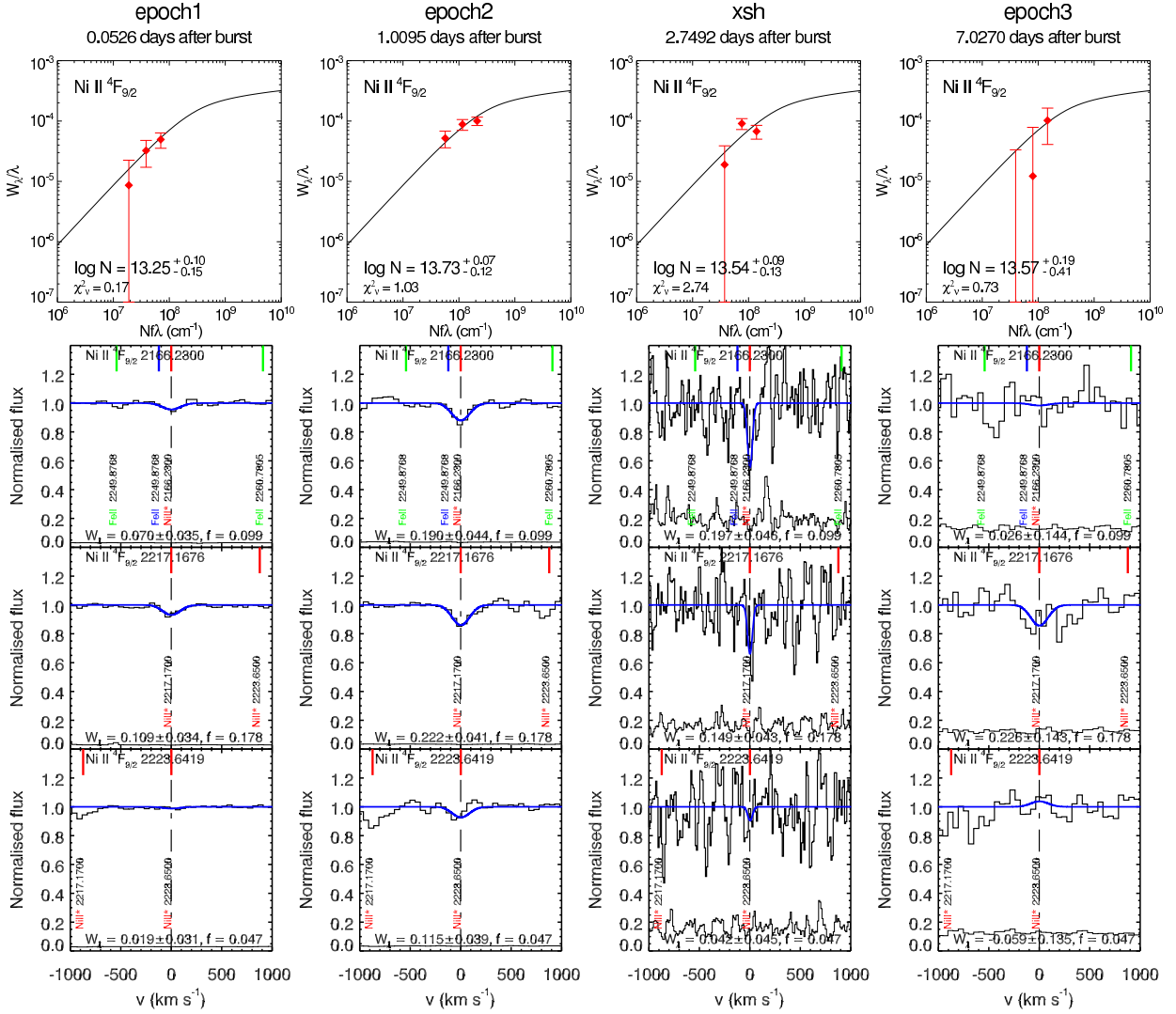
Figure 6. Curves-of-growth (COG) and spectrum excerpts for the three detected lines from the Ni II $^4F_{9/2}$ metastable level. Every column represents an epoch, with the observed time since the burst indicated on top. The upper plot shows the COG for $b = 22.1$ km s^{-1} to which we fit the equivalent widths for the three transitions (red diamonds). The best-fit column density $N_{\rm level}$ is indicated, together with the χ^2_ν of the COG-fit. Below the COG, the three individual lines are displayed on a velocity scale, with the corresponding gaussian line profile fit. The rest frame equivalent width and oscillator strength are indicated. We use the same line label colouring as in Figure 1.

Table 5. Photo-excitation modelling results for the environment of GRB 100901A with different settings. Column (1) extinction A_V in the host galaxy, (2) requirement for the distance d from the burst to the absorber, (3) requirement for the thickness l of the absorbing cloud, (4) fit result d, (5) fit result l, (6) pre-burst column densities of Fe II and (7) Ni II (ground state) and (8) the reduced chi-square of the fit. See also Figure 8.

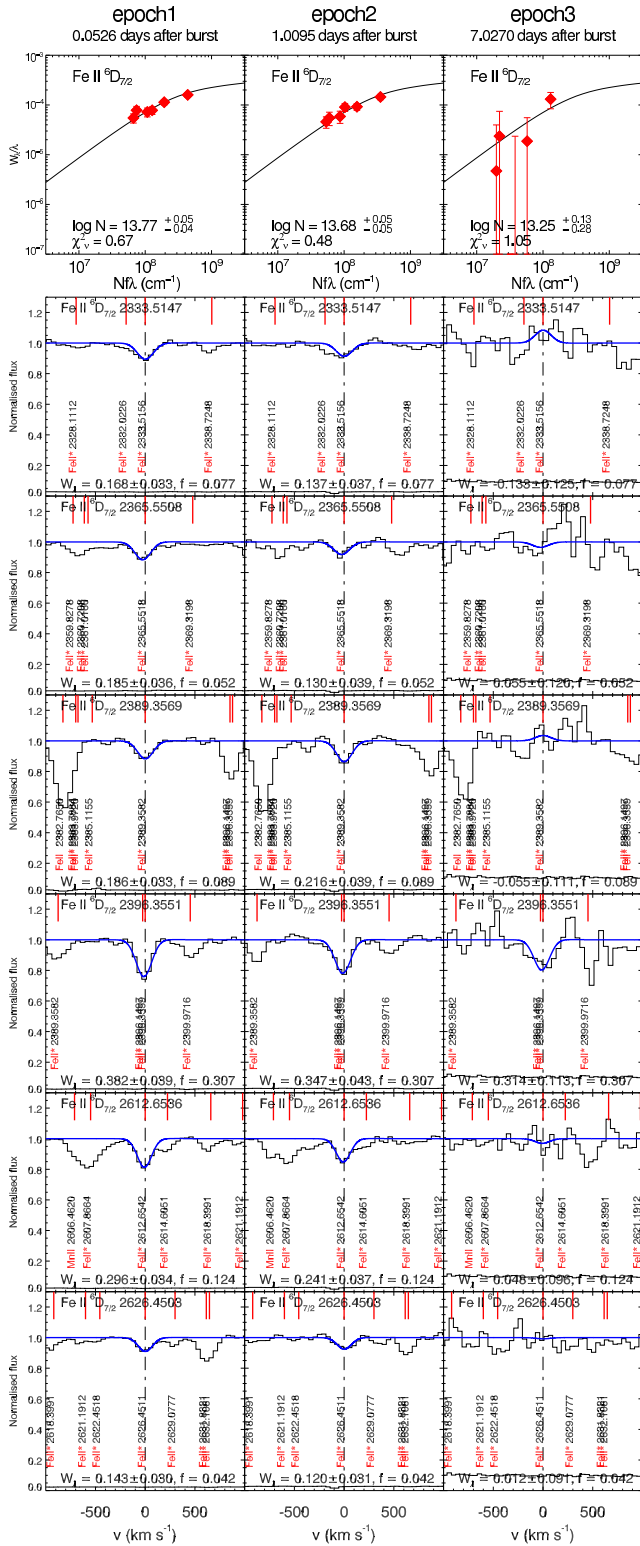| input			output				
A_V	d	l	d/pc	l/pc	$\log\left(N_{\rm Fe\,II}/{\rm cm}^{-2}\right)$	$\log\left(N_{\rm Ni\,II}/{\rm cm}^{-2}\right)$	χ^2_ν
0.0	free	free	250 ± 75	0^{+240}_{-}	$15.25^{+0.05}_{-0.05}$	$13.91^{+0.07}_{-0.08}$	1.54
0.2	minimal 100 pc	free	100^{+61}	1127 ± 569	$15.26^{+0.05}_{-0.06}$	$14.14^{+0.10}_{-0.13}$	0.73
0.2	free	fixed to 1 pc	275 ± 12	1	$15.24^{+0.05}_{-0.06}$	$13.94^{+0.06}_{-0.07}$	1.35
0.2	free	fixed to 100 pc	249 ± 13	100	$15.24^{+0.05}_{-0.06}$	$13.95^{+0.06}_{-0.07}$	1.33
0.2	free	maximal 500 pc	165 ± 73	500^{+}_{-469}	$15.22^{+0.05}_{-0.06}$	$14.02^{+0.10}_{-0.13}$	1.15

Figure 7. The same as Figure 6, only for the six detected lines from the Fe II $^6D_{7/2}$ fine-structure level. We omit the xsh epoch, because for this level none of the lines was significantly detected due to the low S/N.
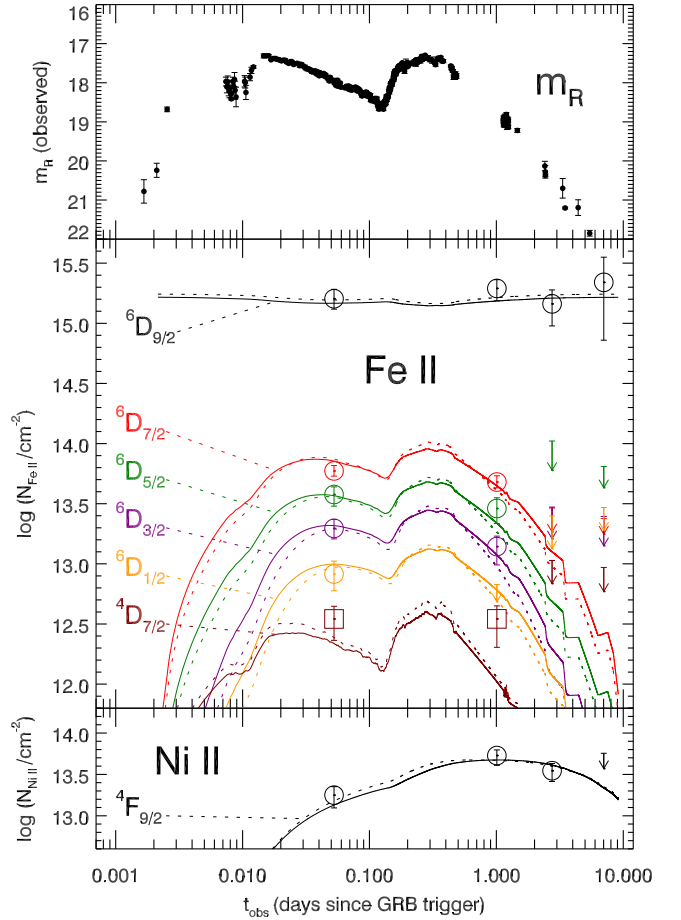

Figure 8. Top panel: observed *R*-band magnitudes from various observatories (see text), which are used as input for the photo-excitation model (see Section 3.2.1). Middle and bottom panel: column density as a function of observed time for Ni II fine-structure and metastable levels, and for the Ni II $^4F_{9/2}$ metastable level. The open circles and squares (arrows) indicate the column densities (limits) derived for each excited state (see Table 4). The solid lines are the predicted best fit result of the photo-excitation model with a maximum absorber thickness $l \leqslant 500\,\mathrm{pc}$ ($\chi_\nu^2 = 1.15$); the dotted line for a model with fixed absorber thickness $l = 1\,\mathrm{pc}$ ($\chi_\nu^2 = 1.35$), both with $A_V = 0.21$.

a large fraction (50%) of the ground-state Fe II is further away does not change the inferred distance much.

3.2.2 Atomic data

In the full analysis from the COG to the photo-excitation model fitting, we need to adopt a set of values for vacuum wavelengths λ and oscillator strengths f_λ. The results of the analysis described in this paper are obtained with the atomic data given in Tables A1, A2, A3 and A4. This atomic parameter set is the same as the one used in CLOUDY (Ferland et al. 1998), a widely-used photo-ionisation code, and comes from Verner et al. (1999) and references therein (see also Ledoux et al. 2009). The choice for this set is in principle arbitrary, but chosen such that our results can easily be compared with other works on GRB afterglow spectra. We tested the dependence of our results to this input by carrying out the full analysis with a different set of values for λ and f_λ. This alternative set is the same as used in Vreeswijk et al. (2007) and uses atomic data from Quinet, Le Dourneuf & Zeippen (1996), Morton (2003) and
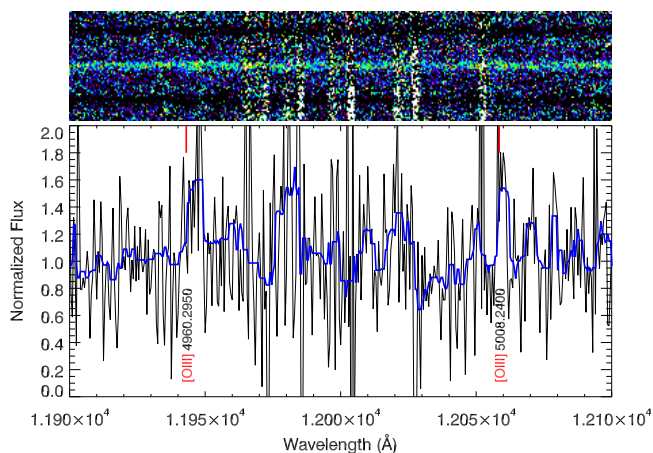
Figure 9. [O III] host emission lines, redshifted to $\sim 1.2\mu$ in the xsh-NIR spectrum. The top panel shows the 2D spectrum (0.5Å/px). The bottom panel shows in black the normalised 1D spectrum (0.5Å/px); in blue the same spectrum, but with a 10 pixel median filter to make the lines easier to see. The non-identified peaks in the 1D spectrum are due to residuals of skyline subtraction which are visible in the 2D spectrum as vertical white strips.

Kurucz (2003). This leads to a 2% lower b, and differences up to 0.06 dex in log $N(t)$. The final resulting l and d of the cloud from the modelling in Section 3.2.1 differ by < 10%, sometimes with lower values for χ_ν^2. This latter fact is, however, not a reason to adopt the alternative set but rather to interpret the scatter in the results as an additional error.

3.3 Emission lines

Because GRBs originate in star forming galaxies, we have searched for emission lines at the host-galaxy redshift. There is tentative evidence for [O III] λ5007 (see Figure 9), of which we estimate the flux to be $4.2 \pm 1.3 \times 10^{-17}$ erg s^{-1} cm^{-2}, error including systematics due to flux calibration. [O III] λ4959 appears to be present, but is blended with a nearby skyline and cannot be measured. We do not detect Hα, Hβ or [O II] due to low S/N and/or skyline blends.

4 DISCUSSION

We have shown that the GRB 100901A afterglow UV radiation excited Fe II and Ni II ions in an absorbing cloud located a few hundred parsecs away in the host-galaxy ISM (Section 3.2). The ionic column densities we derive for the part of this host galaxy that is along the line of sight (Section 3.1) are very comparable to other GRB hosts where fine-structure lines are detected in the afterglow spectra (see e.g., Penprase et al. 2006; Prochaska, Chen & Bloom 2006; Vreeswijk et al. 2007; D'Elia et al. 2009b). Furthermore, the part of the galaxy we probe does not appear to be a special case in the context of dust depletion (Section 3.1.1). Modelling of the variation of the lines from the excited states allows us to estimate the distance to, and the size of, the absorbing cloud. This has been possible for about a dozen of bursts; in the following section we will discuss what these absorber distances teach us about the use of GRB afterglows as probes of galaxies.

4.1 GRBs as probes of galaxies

GRB afterglows are used as probes of their host galaxies, making use of the fact that the afterglow can be extremely bright for a short time. An advantage (for example over galaxies in quasar sight lines) is that afterglows select star-forming galaxies, under the generally accepted assumption that GRBs are linked to (massive) star formation (Woosley 1993; Paczyński 1998). In order to judge how useful they are as galaxy probes, it is important to understand what the influence of the GRB and its afterglow is on the environment, and what part of the host galaxy we are probing. For about a dozen GRB afterglows (see Table 6), the distance between the region where the absorption lines originate and the site where the burst has gone off has been derived with spectroscopy. The typical absorber distance is of the order of a few hundred pc, so the values we find for GRB 100901A appear to be normal (Table 6). These values are also in agreement with lower limits on the absorber distance (> 50 − 100 pc) revealed by the presence of Mg I absorption lines (Prochaska, Chen & Bloom 2006).

Evidently, a GRB is able to affect the ISM out to distances of 100 to 1000 pc, which can be much further out than only the star-forming region of the GRB progenitor. For example, the largest star-forming region in the Local Group, the Tarantula nebula, has a diameter of ~ 200 pc (Lebouteiller et al. 2008). Firstly, this means that the GRB and its afterglow could have considerably influenced the environment it probes. Secondly, the absorption lines that we observe are probably not from the immediate star-forming region of the progenitor of the burst. This is important, as many stellar evolution models that are proposed as long GRB progenitors critically rely on a low metallicity (in particular iron group element abundances, see e.g., Woosley & Heger 2006). Knowing the distance to the abundance-providing cloud gives more quantitative input into the reliability of the found abundances as tracers of the progenitor abundances.

4.2 Can low-R spectra be of use in the analysis of fine-structure line variation?

Our analysis of the fine-structure line variability in GRB 100901A differs from other studies because it is predominantly based on low-resolution spectra, while most other absorber distances are determined from spectra with a $25 - 40$ times higher spectral resolution (see Table 6). Low resolution allowed us to monitor the spectrum over a much longer time-span. We note that GRB 100901A remained particularly bright even after a week. The combination of our observations and the excitation modelling shows that we are detecting the peak of the Ni II $^4F_{9/2}$ level population at around 1 day after the burst in the observer's frame (see Figure 8), which to date has not been observed. The downside is that low-resolution spectroscopy yields less accurate results, because additional steps and assumptions are required to translate equivalent widths to column densities. Furthermore, it is difficult to disentangle different velocity components, limiting the degree to which we can map the internal dynamical structure of the host galaxy.

When a (multi-epoch) low-resolution data set is available, we have shown that it is worthwhile to measure the variation and estimate the absorber distance by fitting a photo-excitation model to it. Especially the lines from the Ni II $^4F_{9/2}$ metastable level have proven to be useful for these kind of long time-span spectroscopic data-sets. These lines are strong, relatively isolated from other common lines in the spectrum, but still close to each other (with GMOS,

one would be able to catch all four of them if the burst is at $0.8 < z < 1.9$), and it takes longer for the levels to depopulate compared to the Fe II fine-structure levels. In terms of recommendations for observing strategies, it would still be most useful to obtain a high-resolution spectrum as soon as possible after the burst, but late-time (after a few days depending on the brightness) spectroscopic follow-up at low resolution can provide additional constraints on the line variation. The information about the different velocity components and their Doppler parameters obtained from the earliest spectrum can be used to interpret the late time low-resolution data more accurately.

5 SUMMARY AND CONCLUSIONS

We have analysed the optical to near-IR spectra of the afterglow of GRB 100901A. Our data set consists of three low-resolution spectra obtained with Gemini-N/GMOS at 1 hour, 1 day and at seven days after the burst, and one medium-resolution VLT/X-shooter spectrum taken nearly 3 days post burst. At a redshift of 1.4084 a wealth of metal resonance and fine-structure lines is detected, allowing us to estimate column densities of Fe, Si, Cr, Mn, Zn, Mg, Ca and Al with a multi-ion single component curve-of-growth (MISC-COG) analysis. The obtained metal column densities are similar to what has been found in many GRB sightlines. Ly-α is not detected, so no metallicity can be determined.

[Fe/Zn] $= -1.13 \pm 0.10$ suggests the presence of dust in the host galaxy. A comparison of the observed dust depletion pattern with sight lines in the Milky Way (Savage & Sembach 1996) reveals a slight preference for a warm-halo-like depletion pattern.

The spectrum shows two intervening absorbers at redshifts 1.3147 and 1.3179. Lines of Fe II, Al II, Al III, Mg I and Mg II have been detected and the corresponding column densities are estimated with the MISC-COG technique. We do not see significant variation in the strength of any of these lines from the intervening absorbers. Under simple assumptions for the projected source size as a function of time, this lack of variability sets a lower limit of 0.03 pc on the size (or homogeneity scale) of the absorbing clouds in these foreground galaxies.

At the host-galaxy redshift we detect lines arising from fine-structure levels of the ground state of Fe II and metastable levels of Fe II and Ni II. The strengths of these lines are found to vary significantly in time. By grouping transitions that arise from the same lower level, we have used the COG from the Fe II resonance lines to retrieve the temporal behaviour of the column density of each of these excited ion species. This information is fed into a photo-excitation model, that uses the rest-frame UV-flux of the burst as input. We assume that the excited levels are populated due to the UV-radiation produced by the afterglow. The model computes the distance between the burst location and the cloud of gas in which the lines originate, and the size of this cloud. For GRB 100901A, we estimate an absorber distance of a few hundred pc, which appears to be typical compared with similar studies.

This is the first time that a fine-structure line variability analysis is predominantly based on low-resolution spectra, and as a consequence of that, also the longest time span over which such variation is detected and modelled. The decrease of the Ni II $^4F_{9/2}$ metastable level population has not been detected before; our data, in combination with our modelling results, show that we cover the peak of the excitation of this level. We argue that applying the fine-structure variability model to low-resolution data can yield a sensible estimate for the absorber distance, but additional intermediate

steps (such as the COG) are necessary, which may cause additional (systematic) errors.

REFERENCES

Andreev M., Sergeev A., Pozanenko A., 2010a, GCN, 11166, 1
—, 2010b, GCN, 11168, 1
—, 2010c, GCN, 11191, 1
—, 2010d, GCN, 11201, 1
Andreev M., Sergeev A., Pozanenko A., Parakhin N., Velichko S., Borachok N., Petkov V., 2010, GCN, 11200, 1
Asplund M., Grevesse N., Sauval A. J., Scott P., 2009, ARAA, 47, 481
Balashev S. A., Petitjean P., Ivanchik A. V., Ledoux C., Srianand R., Noterdaeme P., Varshalovich D. A., 2011, MNRAS, 418, 357
Berger E., Penprase B. E., Cenko S. B., Kulkarni S. R., Fox D. B., Steidel C. C., Reddy N. A., 2006, APJ, 642, 979
Bergeson S. D., Lawler J. E., 1993a, APJL, 414, L137
—, 1993b, APJ, 408, 382
Bohlin R. C., Savage B. D., Drake J. F., 1978, APJ, 224, 132
Chornock R., Berger E., Fox D., Levan A. J., Tanvir N. R., Wiersema K., 2010, GCN, 11164, 1
Cucchiara A., Jones T., Charlton J. C., Fox D. B., Einsig D., Narayanan A., 2009, APJ, 697, 345
Cucchiara A. et al., 2012, ArXiv e-prints
De Cia A. et al., 2012, A&A, 545, A64
de Ugarte Postigo A. et al., 2012, A&A, 548, A11
de Ugarte Postigo A., Thöne C. C., Goldoni P., Fynbo J. P. U., the X-shooter GRB collaboration, 2011, Astronomische Nachrichten, 332, 297
D'Elia V., Campana S., Covino S., D'Avanzo P., Piranomonte S., Tagliaferri G., 2011, MNRAS, 418, 680
D'Elia V. et al., 2010a, MNRAS, 401, 385
—, 2007, A&A, 467, 629
—, 2009a, APJ, 694, 332
—, 2009b, A&A, 503, 437
—, 2010b, A&A, 523, A36

Table 6. Bursts for which an absorber distance has been derived from (the variability of) lines from excited and/or ionised states in the afterglow spectrum. Column (1) Burst ID, column (2) number of epochs, column (3) approximate time (observer's frame) between the different epochs, column (4) telescope and spectrograph with which the data have been taken, columns (5) and (6) the ions and levels/lines for which variability is measured and/or modelled, column (7) redshift of the burst, column (8) neutral hydrogen column density columns (9) and (10) distance between the burst and the region where the lines originate, and size of this region following from modelling of the variability, column (11) reference.

Burst	#	Δt_{obs}	instrument	ion	levels/lines	z_h	$\log N_{HI}$	d/pc	l/pc	ref.
020813	2	~ 16h	KECK/LRIS VLT/UVES	Fe II	$^6D_{7/2}$ $\lambda2396$	1.25	-	$50-100$	-	1
050730	2	~ 1h	VLT/UVES	Fe II	$^6D_{7/2},^6D_{5/2},^6D_{3/2},^6D_{1/2}$, $^4F_{9/2},^4F_{7/2},^4F_{5/2},^4F_{3/2}$, $^4D_{7/2},^4D_{5/2}$	3.97	22.10	124 ± 20	147^{+68}_{-54}	2, 3, 4
051111	1		KECK/HIRES	Fe II Si II	$^6D_{7/2},^6D_{5/2},^6D_{3/2},^6D_{1/2}$, $^2P^°_{3/2}$	1.55	-	a few times 10^2	-	5, 6
060206	2^a		WHT/ISIS	Si II O I C II	$^2P^°_{3/2}$, $^3P^°_0,\,^3P^°_1$, $^2P^°_{3/2}$	4.05	20.85 ± 0.1	$\sim 10^3$	-	7, 8
060418	6	$5-30$ min	VLT/UVES	Fe II Ni II	$^6D_{7/2},^6D_{5/2},^6D_{3/2},^6D_{1/2}$, $^4F_{9/2},^4D_{7/2}$, $^4F_{9/2}$	1.49	-	480 ± 56	-	9, 3
080310	$2-4$	$10-20$ min	VLT/UVES	Fe II Fe III Si II C II	$^6D_{7/2},^6D_{5/2},^6D_{3/2},^6D_{1/2}$, $^4F_{9/2},^4D_{7/2}$, $^5D,\,^7S_3$, $^2P^°_{3/2}$, $^2P^°_{3/2}$	2.43	18.70 ± 0.1	$200-400$	$0-100$	10, 11
080319B	3	$40-60$ min	VLT/UVES	Fe II	$^6D_{7/2},^6D_{5/2},^6D_{3/2},^6D_{1/2}$, $^4F_{9/2},^4F_{7/2}$, $^4D_{7/2},^4D_{5/2}$	0.94	-	$560-1700$	-	12, 3
080330	1		VLT/UVES	Fe II Si II Ni II	$^6D_{7/2},^6D_{5/2},^6D_{3/2},^6D_{1/2}$, $^4F_{9/2}$, $^2P^°_{3/2}$, $^4F_{9/2}$	1.51	-	79^{+11}_{-14}	-	13, 3
081008	4^a	$7-25$ min	VLT/UVES VLT/FORS2	Fe II Si II Ni II	$^6D_{7/2},^6D_{5/2},^6D_{3/2}$, $^4F_{9/2},^4D_{7/2}$, $^2P^°_{3/2}$, $^4F_{9/2}$	1.97	21.11 ± 0.10	52 ± 6 and 200^{+60}_{-80}	-	14
090926	4^a		VLT/X-shooter	Fe II Si II O I C II Ni II	$^6D_{7/2},\,^4F_{9/2}$, $^2P^°_{3/2}$, $^3P^°_0,\,^3P^°_1$, $^2P^°_{3/2}$, $^4F_{9/2}$	2.11	21.60 ± 0.07	677 ± 42 and 5×10^3	-	15, 3
100219A	1		VLT/X-shooter	Si II	$^2P^°_{3/2}$	4.67	21.14 ± 0.15	300 and 10^3		16
100901A	4	1 h - 1 wk	Gemini-N/GMOS VLT/X-shooter	Fe II Ni II	$^6D_{7/2},^6D_{5/2},^6D_{3/2},^6D_{1/2}$, $^4D_{7/2}$, $^4F_{9/2}$	1.41	-	a few times 10^2	$1-1000$	17

^{a}More than one epoch is obtained, but the distance measurement did not follow from modelling the variation.

References: (1) Dessauges-Zavadsky et al. (2006); (2) Ledoux et al. (2009); (3) Vreeswijk et al. (2011); (4) D'Elia et al. (2007); (5) Penprase et al. (2006); (6) Prochaska, Chen & Bloom (2006); (7) Fynbo et al. (2006); (8) Thöne et al. (2008); (9) Vreeswijk et al. (2007); (10) De Cia et al. (2012); (11) Vreeswijk et al. (2013); (12) D'Elia et al. (2009a); (13) D'Elia et al. (2009b); (14) D'Elia et al. (2011); (15) D'Elia et al. (2010b); (16) Thöne et al. (2012); (17) this work.

Dessauges-Zavadsky M., Chen H.-W., Prochaska J. X., Bloom J. S., Barth A. J., 2006, APJL, 648, L89

D'Odorico S. et al., 2006, in Society of Photo-Optical Instrumentation Engineers (SPIE) Conference Series, Vol. 6269, SPIE Conference Series

Elíasdóttir Á. et al., 2009, APJ, 697, 1725

Ellison S. L., Ibata R., Pettini M., Lewis G. F., Aracil B., Petitjean P., Srianand R., 2004, A&A, 414, 79

Ferland G. J., Korista K. T., Verner D. A., Ferguson J. W., Kingdon J. B., Verner E. M., 1998, PASP, 110, 761

Fiore F. et al., 2005, APJ, 624, 853

Fukugita M., Shimasaku K., Ichikawa T., 1995, PASP, 107, 945

Fynbo J. P. U. et al., 2002, in Lighthouses of the Universe: The Most Luminous Celestial Objects and Their Use for Cosmology, Gilfanov M., Sunyeav R., Churazov E., eds., p. 187

—, 2009, APJS, 185, 526

—, 2006, A&A, 451, L47

Goldoni P., Royer F., François P., Horrobin M., Blanc G., Vernet J., Modigliani A., Larsen J., 2006, in Presented at the Society of Photo-Optical Instrumentation Engineers (SPIE) Conference, Vol. 6269, SPIE Conference Series

Gorbovskoy E. S. et al., 2012, MNRAS, 421, 1874

Granot J., Piran T., Sari R., 1999, APJ, 513, 679

Guidorzi C., Cano Z., Melandri A., Kopac D., 2010, GCN, 11160, 1

Hjorth J. et al., 2012, APJ, 756, 187

Immler S. et al., 2010, GCN, 11159, 1

Jenkins E. B., 1986, Astrophyiscal Journal, 304, 739

Kuroda D., Hanayama H., Miyaji T., Watanabe J., Yanagisawa K., Yoshida M., Ohta K., Kawai N., 2010a, GCN, 11205, 1

Kuroda D., Yanagisawa K., Shimizu Y., Toda H., Nagayama S., Yoshida M., Ohta K., Kawai N., 2010b, GCN, 11172, 1

Kurucz R. L., 2003, in IAU Symposium, Vol. 210, Modelling of Stellar Atmospheres, Piskunov N., Weiss W. W., Gray D. F., eds., p. 45

Lebouteiller V., Bernard-Salas J., Brandl B., Whelan D. G., Wu Y., Charmandaris V., Devost D., Houck J. R., 2008, APJ, 680, 398

Ledoux C., Vreeswijk P. M., Smette A., Fox A. J., Petitjean P., Ellison S. L., Fynbo J. P. U., Savaglio S., 2009, A&A, 506, 661

Lu L., Sargent W. L. W., Barlow T. A., Churchill C. W., Vogt S. S., 1996, APJS, 107, 475

Modigliani A. et al., 2010, in Society of Photo-Optical Instrumentation Engineers (SPIE) Conference Series, Vol. 7737, SPIE Conference Series

Morton D. C., 1991, APJS, 77, 119

—, 2003, APJS, 149, 205

Paczyński B., 1998, APJL, 494, L45

Penprase B. E. et al., 2006, APJ, 646, 358

Perna R., Lazzati D., Fiore F., 2003, APJ, 585, 775

Petitjean P., Aracil B., Srianand R., Ibata R., 2000, A&A, 359, 457

Pettini M., Ellison S. L., Steidel C. C., Bowen D. V., 1999, APJ, 510, 576

Pettini M., Ellison S. L., Steidel C. C., Shapley A. E., Bowen D. V., 2000, APJ, 532, 65

Prochaska J. X., 2006, APJ, 650, 272

Prochaska J. X., Chen H., Bloom J. S., 2006, APJ, 648, 95

Prochaska J. X., Chen H., Dessauges-Zavadsky M., Bloom J. S., 2007, ApJ, 666, 267

Prochaska J. X., Wolfe A. M., 1996, APJ, 470, 403

—, 1997, APJ, 474, 140

—, 2000, APJL, 533, L5

Prochaska J. X. et al., 2001, APJS, 137, 21

Prochter G. E. et al., 2006, APJL, 648, L93

Quinet P., Le Dourneuf M., Zeippen C. J., 1996, A&AS, 120, 361

Sakamoto T. et al., 2010, GCN, 11169, 1

Savage B. D., Sembach K. R., 1996, ARAA, 34, 279

Savaglio S., 2006, New Journal of Physics, 8, 195

—, 2012, Astronomische Nachrichten, 333, 480

Savaglio S., Fall S. M., 2004, APJ, 614, 293

Savaglio S., Fall S. M., Fiore F., 2003, APJ, 585, 638

Savaglio S., Glazebrook K., Le Borgne D., 2009, APJ, 691, 182

Schady P., Savaglio S., Krühler T., Greiner J., Rau A., 2011, A&A, 525, A113

Schlegel D. J., Finkbeiner D. P., Davis M., 1998, APJ, 500, 525

Spitzer L., 1978, Physical processes in the interstellar medium. New York Wiley-Interscience, 1978. 333 p.

Thöne C. C. et al., 2012, ArXiv e-prints

—, 2008, A&A, 489, 37

Umeda H., Nomoto K., 2002, APJ, 565, 385

Vacca W. D., Cushing M. C., Rayner J. T., 2003, Publications of the ASP, 115, 389

van Paradijs J. et al., 1997, Nature, 386, 686

Vergani S. D., Petitjean P., Ledoux C., Vreeswijk P., Smette A., Meurs E. J. A., 2009, A&A, 503, 771

Verner D. A., Ferland G. J., Korista K. T., Yakovlev D. G., 1996, APJ, 465, 487

Verner E. M., Verner D. A., Korista K. T., Ferguson J. W., Hamann F., Ferland G. J., 1999, APJS, 120, 101

Vernet J. et al., 2011, ArXiv e-prints

Volnova A., Pozanenko A., E. K., Korobtsev I., 2010, GCN, 11270, 1

Vreeswijk P. M. et al., 2004, A&A, 419, 927

—, 2001, APJ, 546, 672

—, 2013, A&A, 549, A22

—, 2007, A&A, 468, 83

—, 2011, A&A, 532, C3

Watson D. et al., 2006, APJ, 652, 1011

Waxman E., Draine B. T., 2000, APJ, 537, 796

Wiersema K., 2011, MNRAS, 414, 2793

Wolfe A. M., Gawiser E., Prochaska J. X., 2005, ARAA, 43, 861

Woosley S. E., 1993, APJ, 405, 273

Woosley S. E., Heger A., 2006, ApJ, 637, 914

AFFILIATIONS

[1]Astronomical Institute "Anton Pannekoek", University of Amsterdam, P.O. Box 94249, 1090 GE Amsterdam, The Netherlands.

[2]Leiden Observatory, Leiden University, P.O. Box 9513, 2300 RA Leiden, The Netherlands.

[3]University of Leicester, Department of Physics and Astronomy, University Road, Leicester LE1 7RH, United Kingdom

[4]Centre for Astrophysics and Cosmology, Science Institute, University of Iceland, Dunhaga 5, IS-107 Reykjavik, Iceland

[5]Max Planck Institute for Extraterrestrial Physics, 85748 Garching bei München, Germany

[6]Harvard-Smithsonian Center for Astrophysics, 60 Garden Street, Cambridge, MA 02138, USA

[7]INAF - Osservatorio Astronomico di Brera, Via E. Bianchi 46, I-23807 Merate (LC), Italy

[8]INAF-Osservatorio Astronomico di Roma, Via Frascati 33, I-00040 Monteporzio Catone, Italy

[9]ASI-Science Data Centre, Via Galileo Galilei, I-00044 Frascati, Italy

[10]Laboratoire GEPI, Observatoire de Paris, CNRS-UMR8111, Univ Paris Diderot, 5 place Jules Janssen, 92195 Meudon France

[11]Dark Cosmology Centre, Niels Bohr Institute, University of Copenhagen, Juliane Maries Vej 30, DK-2100 Copenhagen, Denmark

[12]APC, Astroparticules et Cosmologie, Universite Paris Diderot, CNRS/IN2P3, CEA/Irfu, Observatoire de Paris, Sorbonne Paris Cite, 10, rue Alice Domon et Leonie Duquet, 75205 Paris Cedex 13, France

[13]Faculty of Mathematics and Physics, University of Ljubljana, Jadranska 19, SI-1000 Ljubljana, Slovenia

[14]Centre of Excellence SPACE-SI, Aškerčeva cesta 12, SI-1000 Ljubljana, Slovenia

[15]Astrophysics Research Institute, Liverpool John Moores University, Twelve Quays House, Egerton Wharf, Birkenhead, CH41 1LD, United Kingdom

[16]Space Research Institute (IKI), 8432 Profsoyuznaya str., Moscow, 117997, Russia

[17]Instituto de Astrofísica de Andalucía (IAA-CSIC), Glorieta de la Astronomía s/n, E-18008, Granada, Spain

APPENDIX A: TABLES WITH LINE TRANSITIONS

Table A1. Lines from the ground state of Fe II (electron configurations $3d^6(^5D)4s - 3d^6(^5D)4p$) and its fine-structure levels, that could in principle be detected in the spectrum of GRB 100901A, because the transition would lie within the GMOS spectral range and the oscillator strength f_λ is not smaller than about 0.005 (except for the $^6D_{9/2}$ resonance lines). The lines of which the wavelengths are in boldface have been used in the modelling reported in Section 3.2. W_λ are measured equivalent widths per epoch, converted to the rest frame.

lower level	$\lambda_{\rm vac}$ (Å)	f_λ	$\log gf$	$J_i - J_k$	terms	W_λ(epoch1)	W_λ(epoch2)	W_λ(xsh)	W_λ(epoch3)
$^6D_{9/2}$	1608.4509	0.05399	-0.268	9/2 − 7/2	$a^6D - y^6P°$	possibly present, but blended with Al II λ1670 at $z = 1.318$.			
0 cm^{-1}	1611.2004	0.00136	-1.867	9/2 − 7/2	$a^6D - z^4F°$	not detected.			
	2249.8754	0.00219	-1.660	9/2 − 7/2	$a^6D - z^4D°$	0.129 ± 0.034	0.151 ± 0.040	0.143 ± 0.044	0.093 ± 0.138
	2260.7793	0.00262	-1.582	9/2 − 9/2	$a^6D - z^4F°$	0.152 ± 0.034	0.168 ± 0.040	0.074 ± 0.060	0.256 ± 0.125
	2344.2129	0.12523	0.098	9/2 − 7/2	$a^6D - z^6P°$	0.748 ± 0.047^a	0.798 ± 0.054^a	0.704 ± 0.189^a	0.557 ± 0.134^a
	2374.4604	0.03297	-0.482	9/2 − 9/2	$a^6D - z^6F°$	0.590 ± 0.045	^{b}	^{b}	^{b}
	2382.7641	0.34321	0.536	9/2 − 11/2	$a^6D - z^6F°$	0.683 ± 0.045	^{b}	^{b,c}	^{b}
	2586.6495	0.07094	-0.149	9/2 − 7/2	$a^6D - z^6D°$	0.705 ± 0.043	0.727 ± 0.048	0.696 ± 0.145	0.629 ± 0.107
	2600.1722	0.24226	0.384	9/2 − 11/2	$a^6D - z^6D°$	0.780 ± 0.045	^{b}	^{b,c}	^{b}

^{a}Blended with lines from $^6D_{1/2}$ and $^4F_{7/2}$, total W_λ is reported.
^{b}W_λ of this resonance line is kept fixed to the value obtained at the first epoch to see the possible variation of the (half-) blended fine-structure lines.
^{c}The line (blend) is clearly saturated, and cannot be fit with gaussian (components) in the X-shooter spectrum.

lower level	$\lambda_{\rm vac}$ (Å)	f_λ	$\log gf$	$J_i - J_k$	terms	W_λ(epoch1)	W_λ(epoch2)	W_λ(xsh)	W_λ(epoch3)
$^6D_{7/2}$	**2333.5147**	0.07776	-0.206	7/2 − 5/2	$a^6D - z^6P°$	0.168 ± 0.034	0.137 ± 0.038	0.051 ± 0.189	−0.134 ± 0.126
384.790 cm^{-1}	**2365.5508**	0.05285	-0.374	7/2 − 7/2	$a^6D - z^6P°$	0.185 ± 0.036	0.130 ± 0.039	0.008 ± 0.222	0.056 ± 0.120
	2383.7873	0.00557	-1.351	7/2 − 5/2	$a^6D - z^6F°$	0.087 ± 0.031	0.071 ± 0.034	^{c}	0.054 ± 0.107
	2389.3569	0.08987	-0.143	7/2 − 7/2	$a^6D - z^6F°$	0.187 ± 0.033	0.216 ± 0.040	−0.085 ± 0.303	−0.056 ± 0.112
	2396.3551	0.30779	0.391	7/2 − 9/2	$a^6D - z^6F°$	0.383 ± 0.040^d	0.348 ± 0.043^d	0.170 ± 0.275^d	0.314 ± 0.114^d
	2599.1457	0.10863	-0.061	7/2 − 5/2	$a^6D - z^DF°$	0.190 ± 0.031	0.096 ± 0.030	^{c}	−0.019 ± 0.096
	2612.6536	0.12485	-0.001	7/2 − 7/2	$a^6D - z^6D°$	0.297 ± 0.035	0.241 ± 0.037	0.012 ± 0.106	0.049 ± 0.096
	2626.4503	0.04266	-0.467	7/2 − 9/2	$a^6D - z^6D°$	0.144 ± 0.030	0.120 ± 0.031	0.095 ± 0.118	0.012 ± 0.092

^{d}Blended with $^6D_{5/2}\lambda$2396.1487, but we assume that the contribution from this line to the total W_λ is negligible.

lower level	$\lambda_{\rm vac}$ (Å)	f_λ	$\log gf$	$J_i - J_k$	terms	W_λ(epoch1)	W_λ(epoch2)	W_λ(xsh)	W_λ(epoch3)
$^6D_{5/2}$	**2328.1100**	0.03760	-0.647	5/2 − 3/2	$a^6D - z^6P°$	0.052 ± 0.031	0.031 ± 0.036	0.064 ± 0.235	0.082 ± 0.132
667.683 cm^{-1}	2349.0215	0.08935	-0.271	5/2 − 5/2	$a^6D - z^6P°$	0.204 ± 0.035^e	0.196 ± 0.038^e	0.081 ± 0.154^e	−0.139 ± 0.114^e
	2381.4877	0.03798	-0.642	5/2 − 7/2	$a^6D - z^6P°$	0.022 ± 0.027	−0.009 ± 0.033	^{c}	−0.004 ± 0.111
	2396.1487	0.01636	-1.008	5/2 − 3/2	$a^6D - z^6F°$	blend with $^6D_{7/2}\lambda$2396.3551, which dominates.			
	2399.9718	0.12522	-0.124	5/2 − 5/2	$a^6D - z^6F°$	0.169 ± 0.032	0.163 ± 0.037	0.071 ± 0.255	0.221 ± 0.124
	2405.6173	0.25103	0.178	5/2 − 7/2	$a^6D - z^6F°$	0.254 ± 0.036^f	0.203 ± 0.039^f	0.005 ± 0.205^f	−0.076 ± 0.102^f
	2607.8658	0.12304	-0.132	5/2 − 3/2	$a^6D - z^6D°$	0.308 ± 0.040^g	0.242 ± 0.043	0.083 ± 0.108	0.007 ± 0.131
	2618.3984	0.04800	-0.541	5/2 − 5/2	$a^6D - z^6P°$	0.112 ± 0.029	0.057 ± 0.031	0.127 ± 0.109	−0.038 ± 0.114
	2632.1077	0.08240	-0.306	5/2 − 7/2	$a^6D - z^6D°$	0.252 ± 0.033^h	0.169 ± 0.035^g	−0.015 ± 0.114^g	0.086 ± 0.088^g

^{e}Blended with $^4F_{9/2}\lambda$2348.8346, this is the total W_λ.
^{f}Blended with $^6D_{3/2}\lambda$2405.1626, this is the total W_λ.
^{g}Blended with Mn II λ2606, but this line's W_λ is fixed after the first epoch.
^{h}Blended with $^6D_{3/2}\lambda$2631.8314, this is the total W_λ.

lower level	$\lambda_{\rm vac}$ (Å)	f_λ	$\log gf$	$J_i - J_k$	terms	W_λ(epoch1)	W_λ(epoch2)	W_λ(xsh)	W_λ(epoch3)
$^6D_{3/2}$	**2338.7238**	0.09840	-0.405	3/2 − 3/2	$a^6D - z^6P°$	0.090 ± 0.032	0.057 ± 0.036	0.127 ± 0.174	0.062 ± 0.128
862.613 cm^{-1}	2359.8270	0.06788	-0.566	3/2 − 5/2	$a^6D - z^6P°$	part of a strongly blended complex, with a contribution of an unidentified line.			
	2405.1626	0.02784	-0.953	3/2 − 1/2	$a^6D - z^6F°$	blend with $^6D_{5/2}\lambda$2405.6173, which dominates.			
	2407.3934	0.15988	-0.194	3/2 − 3/2	$a^6D - z^6F°$	0.122 ± 0.032	0.078 ± 0.033	0.014 ± 0.199	0.014 ± 0.112
	2411.2522	0.21967	-0.056	3/2 − 5/2	$a^6D - z^6F°$	0.227 ± 0.035^i	0.115 ± 0.037^i	0.181 ± 0.170^i	0.031 ± 0.089^i
	2614.6047	0.11018	-0.356	3/2 − 1/2	$a^6D - z^6D°$	0.119 ± 0.029	0.091 ± 0.032	0.007 ± 0.105	0.055 ± 0.095
	2621.1906	0.00364	-1.837	3/2 − 3/2	$a^6D - z^6D°$	0.047 ± 0.028	−0.016 ± 0.032	0.035 ± 0.114	0.022 ± 0.084
	2631.8314	0.12430	-0.303	3/2 − 5/2	$a^6D - z^6D°$	blended with $^6D_{5/2}\lambda$2632.1077, see there for the total W_λ.			

^{i}Blended with $^6D_{1/2}\lambda$2411.8009, this is the total W_λ.

lower level	$\lambda_{\rm vac}$ (Å)	f_λ	$\log gf$	$J_i - J_k$	terms	W_λ(epoch1)	W_λ(epoch2)	W_λ(xsh)	W_λ(epoch3)
$^6D_{1/2}$	2344.9996	0.16819	-0.473	1/2 − 3/2	$a^6D - z^6P°$	blended with $^6D_{9/2}\lambda$2344.214 and $^4F_{7/2}\lambda$2344.6789, see there for the total W_λ.			
977.053 cm^{-1}	2411.8009	0.22500	-0.347	1/2 − 1/2	$a^6D - z^6F°$	blended with $^6D_{3/2}\lambda$2411.2522, see there for the total W_λ.			
	2414.0437	0.19047	-0.419	1/2 − 3/2	$a^6D - z^6F°$	0.060 ± 0.030	0.028 ± 0.034	−0.081 ± 0.159	0.073 ± 0.125
	2622.4513	0.05454	-0.962	1/2 − 1/2	$a^6D - z^6D°$	0.036 ± 0.025	0.024 ± 0.029	0.114 ± 0.109	0.116 ± 0.114
	2629.0769	0.17451	-0.457	1/2 − 3/2	$a^6D - z^6D°$	0.079 ± 0.027	0.033 ± 0.031	0.008 ± 0.172	0.119 ± 0.109

Table A2. The same as Table A1, only for the lines from the metastable states of Fe II with electron configuration $3p^6 3d^7$.

lower level	λ_{vac} (Å)	f_λ	$\log gf$	$J_i - J_k$	terms	W_λ(epoch1)	W_λ(epoch2)	W_λ(xsh)	W_λ(epoch3)
$^4F_{9/2}$	1610.9234	0.00914	-1.039	9/2 – 9/2	$a^4F - y^4G°$	not detected, hardly in range, noisy region.			
1872.567 cm^{-1}	1637.3998	0.01418	-0.848	9/2 – 7/2	$a^4F - x^4D°$	not detected, noisy region with many possible lines.			
	1702.0453	0.05316	-0.274	9/2 – 11/2	$a^4F - z^4G°$	possibly detected, but shifted and blended with Ni IIλ1703, noisy region.			
	2332.0235	0.01787	-0.748	9/2 – 7/2	$a^4F - z^4F°$	0.052 ± 0.029	0.085 ± 0.037	0.109 ± 0.199	0.103 ± 0.123
	2348.8346	0.03653	-0.437	9/2 – 7/2	$a^4F - z^4D°$	blended with $^6D_{5/2}\lambda$2349.0215, see there for total W_λ.			
	2360.7213	0.02289	-0.640	9/2 – 9/2	$a^4F - z^4F°$	part of a strongly blended complex, with a contribution of an unidentified line.			
$^4F_{7/2}$	1625.5231	0.02481	-0.702	7/2 – 9/2	$a^4F - y^4G°$	not detected, noisy region.			
2430.097 cm^{-1}	2344.6790	0.01669	-0.874	7/2 – 5/2	$a^4F - z^4F°$	blended with $^6D_{9/2}\lambda$2344.214 and $^6D_{1/2}\lambda$2344.9996, see there for the total W_λ.			
	2361.0161	0.03053	-0.612	7/2 – 5/2	$a^4F - z^4D°$	part of a strongly blended complex, with a contribution of an unidentified line.			
	2380.0023	0.01732	-0.858	7/2 – 7/2	$a^4F - z^4D°$	not detected.			
$^4F_{5/2}$	1633.9093	0.02620	-0.803	5/2 – 7/2	$a^4F - y^4G°$	not detected, noisy region with many possible lines.			
2837.950 cm^{-1}	2369.3195	0.02918	-0.757	5/2 – 3/2	$a^4F - z^4D°$	not detected.			
	2383.9718	0.02215	-0.876	5/2 – 5/2	$a^4F - z^4D°$	blended with many lines including the saturated $^6D_{9/2}\lambda$2382.7641.			
$^4F_{3/2}$	2375.9188	0.03512	-0.852	3/2 – 1/2	$a^4F - y^4D°$	0.061 ± 0.034^j	0.066 ± 0.034^j	-0.147 ± 0.202^j	-0.079 ± 0.100^j
3117.461 cm^{-1}	2385.1148	0.02311	-1.034	3/2 – 3/2	$a^4F - y^4D°$	not detected, close to complex blend.			

^{j}Half-blended with $^6D_{9/2}\lambda$2374.4604, which's W_λ is fixed from the first epoch.

Table A3. The same as Table A1, only for the lines from the metastable states of Fe II with electron configuration $3d^6(^5D)4s$.

lower level	λ_{vac} (Å)	f_λ	$\log gf$	$J_i - J_k$	terms	W_λ(epoch1)	W_λ(epoch2)	W_λ(xsh)	W_λ(epoch3)
$^4D_{7/2}$	1635.4005	0.06857	-0.261	7/2 – 5/2	$a^4D - x^4P°$	heavily blended, noisy region.			
7955.299 cm^{-1}	**2563.3039**	0.13520	0.034	7/2 – 5/2	$a^4D - z^4P°$	0.037 ± 0.027	0.064 ± 0.032	-0.052 ± 0.248	0.047 ± 0.110
	2715.2173	0.04543	-0.440	7/2 – 5/2	$a^4D - z^4D°$	not detected.			
	2740.3577	0.25107	0.303	7/2 – 7/2	$a^4D - z^4D°$	0.056 ± 0.026	0.027 ± 0.029	0.018 ± 0.099	0.114 ± 0.094
	2756.5512	0.30759	0.391	7/2 – 9/2	$a^4D - z^4F°$	0.050 ± 0.025	0.056 ± 0.030	0.097 ± 0.114	-0.045 ± 0.104
$^4D_{5/2}$	1641.7631	0.04742	-0.546	5/2 – 3/2	$a^4D - x^4P°$	blended, noisy region.			
8391.938 cm^{-1}	1647.1625	0.02026	-0.915	5/2 – 5/2	$a^4D - x^4P°$	blended, noisy region.			
	2564.2441	0.09332	-0.252	5/2 – 3/2	$a^4D - z^4P°$	not detected.			
	2592.3179	0.05219	-0.504	5/2 – 5/2	$a^4D - z^4P°$	not detected.			
	2728.3467	0.06890	-0.384	5/2 – 3/2	$a^4D - z^4D°$	not detected.			
	2747.7942	0.18791	0.052	5/2 – 5/2	$a^4D - z^4D°$	part of strongly blended complex.			
	2750.1347	0.32808	0.294	5/2 – 5/2	$a^4D - z^4F°$	blended with $^4D_{3/2}\lambda$2749.9938 and $^4D_{1/2}\lambda$2750.2989.			
$^4D_{3/2}$	2567.6820	0.05684	-0.643	3/2 – 1/2	$a^4D - z^4P°$	not detected.			
8680.454 cm^{-1}	2583.3564	0.08345	-0.477	3/2 – 3/2	$a^4D - z^4P°$	not detected.			
	2731.5431	0.02964	-0.926	3/2 – 3/2	$a^4D - z^4F°$	not detected.			
	2737.7761	0.06574	-0.580	3/2 – 1/2	$a^4D - z^4D°$	not detected.			
	2747.2958	0.35475	0.152	3/2 – 5/2	$a^4D - z^4F°$	part of strongly blended complex.			
	2749.9938	0.13492	-0.268	3/2 – 3/2	$a^4D - z^4D°$	blended with $^4D_{5/2}\lambda$2750.1344 and $^4D_{1/2}\lambda$2750.2988.			
$^4D_{1/2}$	2578.6940	0.12362	-0.607	1/2 – 1/2	$a^4D - z^4P°$	not detected.			
8846.768 cm^{-1}	2744.0089	0.44026	-0.055	1/2 – 3/2	$a^4D - z^4F°$	possibly detected, but half blended Mg I λ2853 at $z = 1.315$.			
	2750.2989	0.12021	-0.619	1/2 – 1/2	$a^4D - z^4D°$	blended with $^4D_{5/2}\lambda$2750.1347 and $^4D_{3/2}\lambda$2749.9938.			

Table A4. The same as Table A1, only for the lines from the metastable states of Ni II with electron configurations $3p^6 3d^8(^3F)4s$.

lower level	λ_{vac} (Å)	f_λ	$\log gf$	$J_i - J_k$	terms	W_λ(epoch1)	W_λ(epoch2)	W_λ(xsh)	W_λ(epoch3)
$^4F_{9/2}$	**2166.2300**	0.09990	0.000	9/2 – 9/2	$^4F - {}^2F°$	0.070 ± 0.035	0.191 ± 0.045	0.197 ± 0.046	0.026 ± 0.145
8393.90 cm^{-1}	**2217.1676**	0.17865	0.252	9/2 – 11/2	$^4F - {}^4G°$	0.110 ± 0.035	0.222 ± 0.042	0.150 ± 0.043	0.227 ± 0.143
	2223.6419	0.04789	-0.320	9/2 – 9/2	$^4F - {}^4G°$	0.019 ± 0.031	0.116 ± 0.039	0.042 ± 0.046	-0.060 ± 0.136
	2316.7481	0.11073	0.044	9/2 – 7/2	$^4F - {}^4D°$	blended with a skyline.			